Journal of Materials Science & Technology 219 (2025) 59–74

Contents lists available at ScienceDirect

Journal of Materials Science & Technology

journal homepage: www.elsevier.com/locate/jmst

Research Article

Triethoxysilane-derived silicon quantum dots: A novel pathway to small size and high crystallinity

Yizhou He[a,b,1], Qianxi Hao[a,b,1], Xue Yang[c,*], Jiamin Yu[c], Chi Zhang[a,b], Ruoyu Li[a,b], Qi Wang[a,b], Shaorong Li[a], Xiaowei Guo[a,b,*], Serguei K. Lazarouk[d]

[a] School of Optoelectronic Science and Engineering, University of Electronic Science and Technology of China (UESTC), Chengdu 610054, China
[b] Yangtze Delta Region Institute (Huzhou), University of Electronic Science and Technology of China (UESTC), Huzhou 313001, China
[c] China National Tobacco Corporation Sichuan Company, Chengdu 610041, China
[d] Belarusian State University of Informatics and Radioelectronics, P. Browka 6, Minsk 220013, Belarus

ARTICLE INFO

Article history:
Received 30 December 2023
Revised 5 September 2024
Accepted 6 November 2024
Available online 16 November 2024

Keywords:
Silicon quantum dots
Network structure
Cross-linking density
Crystalline fraction
Photoluminescence
HSQ polymers

ABSTRACT

The crystalline fraction is a critical parameter for assessing the quality of silicon quantum dots (SiQDs), and its enhancement is anticipated to improve the optoelectronic performance of these materials. However, achieving a high crystalline fraction in small-sized SiQDs produced through the pyrolysis of hydrogen silsesquioxane (HSQ) polymers remains a significant challenge. In this study, we successfully synthesized SiQDs with a diameter of 3.24 nm and a crystalline fraction of 98.4% by optimizing the triethoxysilane (TES)/aqueous hydrochloric acid (HCl) volume ratio during the hydrolysis-condensation process. The SiQDs exhibited a photoluminescence (PL) center at 764.1 nm and an average PL quantum yield (PLQY) of 24.4%. Our findings demonstrate that the TES/aqueous HCl volume ratio significantly influences the proportion of cage structure and the cross-linking density of the network structure in HSQ polymers, which in turn governs SiQD size and crystalline fraction. A high proportion of cage structures in HSQ polymers contributes to high crystallinity. Notably, an increased cross-linking density within the network structure results in higher and more uniform diffusion barriers. This phenomenon not only hinders the diffusion of silicon atoms, which leads to smaller SiQD size, but also facilitates the achievement of high crystalline fraction due to uniform diffusion. This work presents a novel approach to achieving high crystallinity in small SiQDs, with implications for advanced applications in lighting, display technologies, medical imaging, and photovoltaics.

1. Introduction

Driven by the Sustainable Development Goals (SDGs), scientists are dedicated to finding a low-cost and non-toxic luminescent material to replace the rare-earth phosphors widely used today. Silicon (Si), the second most abundant and environmentally friendly element in the earth's crust, has naturally been considered [1]. However, bulk silicon with an indirect bandgap only achieves a photoluminescence quantum yield (PLQY) of ~0.01%, and the photoluminescence (PL) wavelength is only in the near-infrared (NIR) region (~1100 nm) [2]. Silicon quantum dots (SiQDs), a form of Si with dimensions comparable to the Bohr radius (α_B) of an exciton, have wider bandgaps and quasi-direct transition properties with respect to bulk Si [3,4]. SiQDs have been proven to exhibit PL in the region of 400–1050 nm and PLQY as high as ~60% [5–10]. Such excellent PL properties, coupled with the inherent abundance and non-toxicity of Si, make SiQDs expected to shine in applications such as biomedical imaging [11,12], display [13–15], lighting [16–18], and photovoltaics [19,20].

Researchers have developed various physical and chemical routes to synthesize SiQDs, including pulsed laser ablation of solid Si [21–26], plasma synthesis from silane gas [27–29], electrochemical Si wafer etching [30–32], reduction reactions of halosilanes [33–36], and thermal pyrolysis of silicon-rich oxide compounds [6,9,37–45]. Of these routes, thermal pyrolysis is a facile and effective way to synthesize SiQDs with high PLQYs. In 2006, as an initial study, Veinot et al. [6] synthesized SiQDs using pyrolysis of hydrogen silsesquioxane (HSQ) and altered the PL wavelength (red, orange, yellow, and green) by varying the etching time. Subsequent studies on HSQ-derived SiQDs focused on the functional-

* Corresponding authors.
E-mail addresses: 202211050822@std.uestc.edu.cn (Y. He), 202221050717@std.uestc.edu.cn (Q. Hao), 280055419@qq.com (X. Yang), gxw@uestc.edu.cn (X. Guo).
[1] These authors contributed equally to the work.

https://doi.org/10.1016/j.jmst.2024.11.002
1005-0302/

ization of the surface ligands, which extended the PL wavelength region to 400–1050 nm and elevated the PLQY to ~60% in the solution phase (65% in the solid phase) [40,45]. Despite exciting advances in HSQ pyrolysis, the high cost of HSQ and the shutdown of the largest HSQ supplier have hindered the industrialization process of this method [46,47]. As a low-cost alternative, HSQ polymer with a structure similar to HSQ has been proposed. Unlike an HSQ purchased directly from a supplier, HSQ polymer is synthesized by a hydrolysis-condensation reaction with trimethoxysilane (TMS) or triethoxysilane (TES) [48,49], thus offering 380 times lower cost than HSQ [44,46,47]. As an initial study using HSQ polymer, Pauthe et al. synthesized silicon nanocrystals with diameters ranging from 5–20 nm by pyrolysis of TES-derived HSQ polymers [48]. Since then, researchers have conducted extensive synthesis and application studies on the SiQDs synthesized from HSQ polymer [5,8,11–17,46,49–57], such as modulation of the PL wavelength of SiQDs by altering the pyrolysis temperature [5,8,49–53], functionalization of the surface ligands [54–56], size separation [57], NIR biological imaging [11,12], and light-emitting diode (LED) device [13–17]. Nevertheless, the PLQYs of polymer-derived SiQDs are generally lower than those of their HSQ counterparts [12,40,45,58], which is attributed to the structural distinction between HSQ polymer and HSQ. HSQ polymer is a mixture of cage and network structures, and the ratio of the two structures is determined by the hydrolysis-condensation reaction conditions [46,49].

To the best of our knowledge, up to now, only four studies have investigated the mechanism of the hydrolysis-condensation reaction for generating HSQ polymer [46,49,52,59]. In 2009, Henderson et al. [49] found that the cross-linking density of HSQ polymers is larger than that of HSQ, which increases the energetic barrier for the diffusion of Si atoms through the oxide matrix, resulting in the formation of smaller SiQDs. In 2017, Xin et al. [52] showed that varying the reaction conditions of $HSiCl_3$ with water in hexane can change the network-cage ratio of HSQ polymers, thus controlling the size of the synthesized SiQDs. In 2020, Terada et al. [46] indicated that the cross-linking density of HSQ polymers is influenced by the amount of methanol used during the hydrolysis-condensation reaction. Specifically, higher methanol/water ratios, which correspond to lower cross-linking densities, result in larger sizes and higher crystallinity of SiQDs. They synthesized SiQDs with sizes of 3.4, 3.6, and 4.6 nm, which correspond to crystalline fractions of 27%, 50%, and 54%, respectively [46]. Recently, Ueda et al. [59] synthesized red-emitting SiQDs with an average diameter of 2.4 nm and a crystalline fraction of 90% using HSQ polymers derived from the hydrolysis of $HSiCl_3$ in combination with weakly polar solvents as precursors. Owing to the high crystalline fraction and effective surface passivation, the PLQY of the SiQDs reached approximately 80%, establishing a new record for the PLQY of SiQDs synthesized via HSQ polymers [59,60]. Although the size and crystallinity of SiQDs can be adjusted to some extent by modifying the synthesis conditions of HSQ polymers, the accompanying crystallinity is often compromised when targeting smaller SiQDs [1,46]. To the best of our knowledge, the crystalline fraction of SiQDs below 3.5 nm remains limited to below 92%, indicating substantial room for improvement [46,47,59]. Enhanced crystallinity can contribute to further increasing the PLQY of SiQDs.

Herein, we present the synthesis of high-crystallinity small SiQDs by varying the TES/aqueous hydrochloric acid (HCl) ratio during the hydrolysis-condensation process. The HSQ polymers before and after pyrolysis were characterized using Fourier transform infrared (FTIR) spectroscopy, X-ray diffraction (XRD), Raman spectroscopy, X-ray photoelectron spectroscopy (XPS) to obtain the cross-linking densities, the percentage of cages and network structures, crystal sizes, the crystallinity fractions, the stress on the SiQDs, and the O/Si ratios. Combining the characterization of SiQDs by transmission electron microscopy (TEM) and PL spectroscopy, we demonstrated that SiQDs can be synthesized from TES-derived HSQ polymers while maintaining small size characteristics and achieving a crystalline fraction close to 100%. Our study sheds light on how the HSQ polymer structure affects the size and crystallinity of SiQDs, offering a new way to generate high-crystallinity small SiQDs by pyrolysis reaction.

2. Experimental section

2.1. Materials

Triethoxysilane (97%), hydrofluoric acid (AR, 48%), 1-octadecene (GC, ≥ 95%), and 1,3,5-Trimethylbenzene (AR, 97%) were purchased from Macklin. Hydrochloric acid (AR, 37%), ethanol (AR, 99.7%), toluene (AR, 99.5%) were purchased from Keshi, a Sichuan local company.

2.2. Synthesis of SiQDs

(1) Hydrolysis-condensation: 20 mL of TES was loaded into a beaker with a magnetic rotor and stirred for 1 h, then 10 mL, 20 mL, 30 mL, or 40 mL of aqueous HCl (pH = 3) was added, with a TES/aqueous HCl volume ratio of 2, 1, 0.67, or 0.5, respectively. Stirring was continued for 10 min until a gel-like product was formed. The gel-like product was placed on a hot plate, heated at 65 °C for 12 h, then dried at room temperature for 24 h to form dry HSQ polymers. The entire hydrolysis-condensation process was carried out in a glove box filled with argon gas.

(2) Thermal Pyrolysis: The HSQ polymers were placed in a quartz boat and fed into a tube furnace heated with a 5% H_2/95% Ar atmosphere. Before heating, the tube furnace was first swept at room temperature for 30 min, then heated to 300 °C at a rate of 5 °C min^{-1}, then to 600 °C at a rate of 10 °C min^{-1}, and kept for 15 min. Finally, the tube furnace was heated to 1000 °C at a rate of 10 °C min^{-1} and held for 2 h. The pyrolysis product was ground into powder.

(3) HF etching: It is essential to emphasize that hydrofluoric acid (HF) utilized in this procedure is highly corrosive and presents a significant risk to human safety. Therefore, stringent precautions must be observed when handling HF. 300 mg of the powder was added to a polytetrafluoroethylene (PTFE) container with 16 mL of HF and 8 mL of ethanol and stirred magnetically at room temperature for 45 min. Then, the solution was centrifuged at 12,000 rpm for 10 min. The supernatant was discarded while the precipitate was kept. The precipitate was subsequently dissolved in ethanol and centrifuged at 12,000 rpm for 10 min, and the supernatant was discarded again. The resulting precipitate was further dried for 12 h to obtain hydrogen-passivated SiQD powder. The entire etching process was carried out in a glove box filled with argon gas.

(4) Hydrosilylation: The hydrogen-passivated SiQDs powder was added to a three-necked flask containing 18 mL of 1-octadecene and 18 mL of mesitylene, and heated for 16 h in an oil bath at 130 °C. The color of the solution changed from colorless to orange-yellow. When the solution was cooled to room temperature, 30 mL of ethanol was added, producing a turbid solution instantly. The yellow turbid solution was centrifuged at 12,000 rpm for 20 min, and the supernatant was discarded. The precipitate was then mixed with 25% toluene/75% ethanol and centrifuged at 12,000 rpm for 5 min when the supernatant was discarded. The precipitate was dried for 12 h and dispersed into toluene to obtain an octadecyl-passivated SiQD solution. The entire hydrosilylation process was carried out in a glove box filled with argon gas.

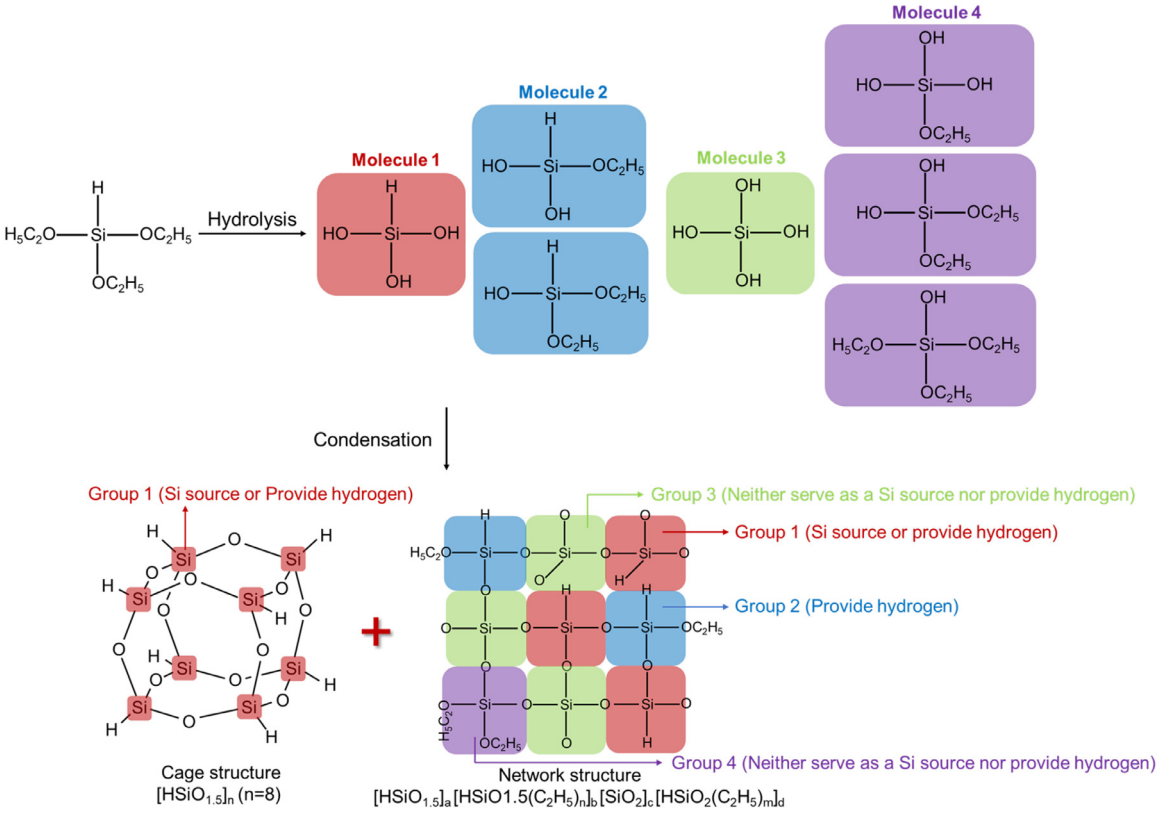

Fig. 1. Schematic diagram of the hydrolysis-condensation reaction of TES.

2.3. Characterization

FTIR spectra were recorded on a Nicolet Is5 spectrometer (Thermo Fisher Scientific) using the attenuated total reflection module with a resolution of 0.48 cm^{-1}. XRD patterns were collected using an Ultima IV diffractometer (Rigaku) with CuKa radiation and a resolution of 5° min^{-1}. Raman scattering measurements were performed using a DXR3 Raman spectrometer (Thermo Scientific) equipped with a confocal microscope; The excitation wavelength and spectral resolution of Raman scattering spectra for pyrolysis products (freestanding octadecyl-passivated SiQDs) were 532 nm (633 nm) and 0.4821 cm^{-1}; The diameter of the laser spot was 2 μm, the laser power was 1.5 mW and the integration time was 30 s. For the Raman measurement of freestanding SiQDs, a dispersion of SiQDs in toluene (2 mg mL^{-1}) was deposited onto a stainless-steel plate to create a film that serves as a sample for Raman spectroscopy measurements. XPS measurements were performed on an Escalab 250Xi XPS system (Thermo Fisher Scientific) using a monochromated Al Ka X-ray source ($h\nu$ = 1486.6 eV). The background pressure of the analysis chamber is lower than 8 × 10^{-10} mbar and that of the sample chamber is lower than 2 × 10^{-8} mbar in standby mode. To remove carbon and oxide contamination from the surface, the samples were subjected to 4 keV Ar^+ ion sputtering for 30 s. TEM, high-resolution transmission electron microscopy (HR-TEM), and selected area electron diffraction (SAED) measurements were performed with a Talos F200S G2 (Thermo Fisher Scientific), operating at an acceleration voltage of 200 kV. Ultraviolet and visible absorption spectra (UV–Vis) were measured with a Shimadzu UV 3600 spectrophotometer equipped with an integrating sphere. PL spectra and PLQYs were determined on a Fluorolog-3 spectrofluorometer (Horiba Scientific) with an integrating sphere (IS80, Labsphere) and a 450 W Xenon Lamp as the excitation source (λ_{ex} = 330 nm for PLQY measurement) and a CCD (SYNAPSE) as the detector. PL decay lifetimes were measured on a Fluorolog-3 spectrofluorometer (Horiba Scientific) with a SpectraLED (355 nm, S-355) as the excitation source and a picosecond photon detection module (PPD-850) as the detector (λ_{em} = 750 nm).

3. Results and discussions

As shown in Fig. 1, TES reacts with aqueous HCl in a hydrolysis-condensation process, which includes two steps. The hydrolysis reaction yields four types of HSQ polymers, in which only type 1 can serve as a silicon source for the subsequent reactions to generate SiQDs. The condensation reaction condenses two Si–OH groups into a Si–O–Si group, resulting in the formation of H_2O as a byproduct and polymers with cage or network structures [44,49].

In this work, we focus on the role of the TES/aqueous HCl volume ratio in the hydrolysis-condensation reaction on the formation of SiQDs. Four cases were considered. The volume ratios for the four cases, stated in order, are 2, 1, 0.67, and 0.5, corresponding to series 1, series 2, series 3, and series 4, respectively, as presented in Table 1. Fig. 2(a, b) shows the FTIR spectra of the HSQ polymers and pyrolysis products. It is observed that the HSQ polymers have three bands of 700–900 cm^{-1}, 900–1300 cm^{-1}, and 2250 cm^{-1}, which are attributed to the H–Si–O bending mode, Si–O–Si stretching mode, and H–Si stretching mode, respectively. The FTIR spectra of the HSQ polymers are in good agreement with those previously reported in the literature [12,49,52,61]. The absence of the Si–H bands in the spectra of the pyrolysis products and the substantial reduction in the intensity of the H–Si–O bands indicate that group 1 in the HSQ polymers has been sufficiently converted to SiQDs. As shown in the insets of Fig. 2(a), HSQ polymers in series 1–3 appear as transparent, lumpy icing sugar, whereas those in series 4 present as a pure white fine powder. Fig. 2(c–f) shows the local zoom-in of the FTIR spectra of the

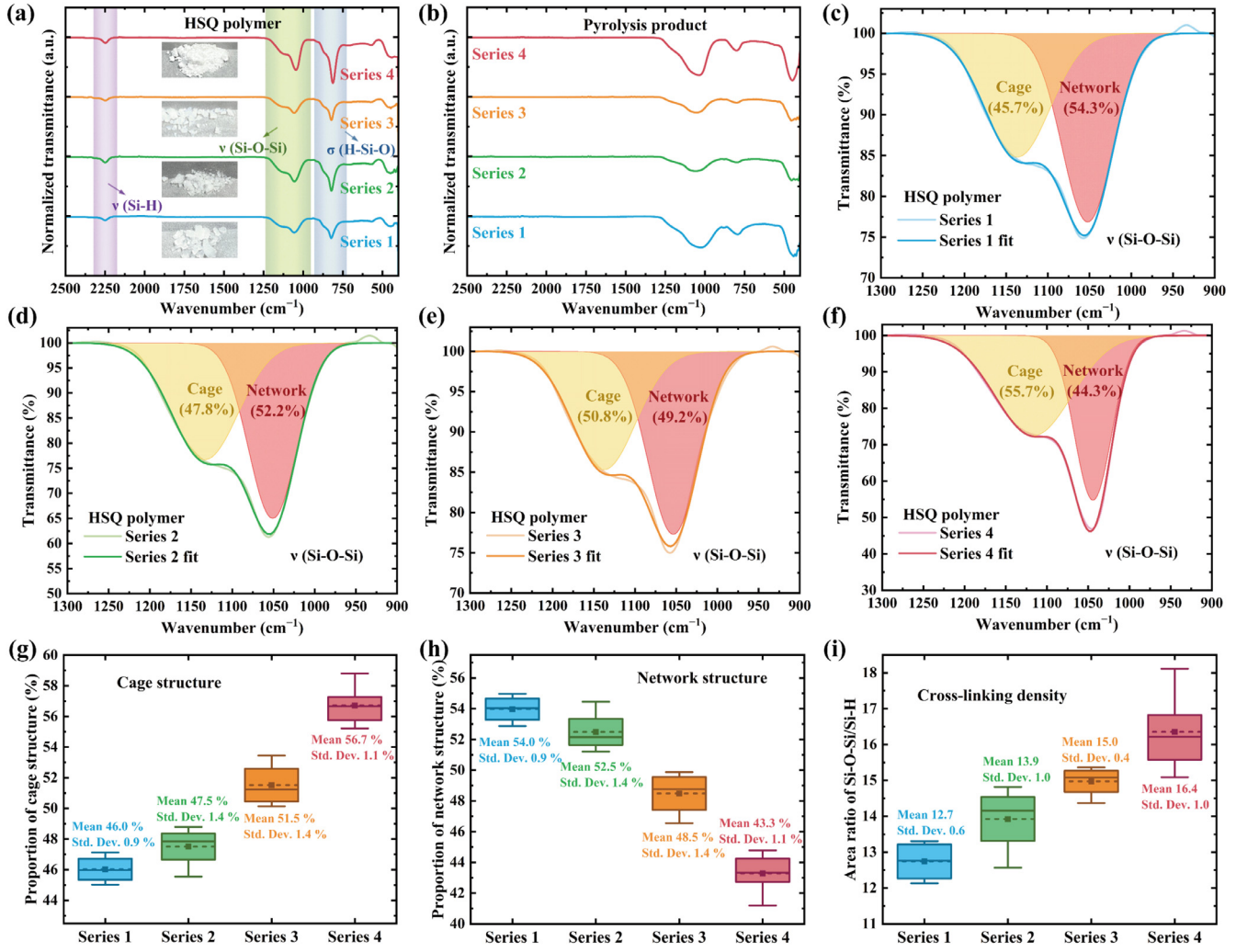

Fig. 2. (a–f) FTIR spectra of HSQ polymers and pyrolysis products of series 1–4 and their local magnified images; (g, h) Box plots of the percentage of the cage and network structures in the HSQ polymers (solid lines within the boxes represent the median, while dashed lines indicate the mean); (i) Box plots of the ratio of the integrated areas of the Si–O–Si bands to the H–Si bands in the HSQ polymers.

series 1–4 HSQ polymers at 900–1300 cm^{-1}. The Si–O–Si bands are fitted to two sub-bands with peaks at 1040–1060 cm^{-1} and 1110–1140 cm^{-1} by Gaussian function, which are assigned to the network and cage structures, respectively [46,49]. The raw data with the baselines fitted by cubic function, which agrees with the methodology reported in the literature [46]. The percentage of the network and cage structures in the HSQ polymers can be obtained using the relative integrated intensity of the two sub-bands, as shown in Fig. 2(g, h) and Table 1. It is important to note that the solid line in the box plot represents the median, while the dashed line signifies the mean; this convention is consistent in the subsequent box plot. As the TES/H_2O volume ratio decreases from series 1 to series 4, the average percentage of cage structures in HSQ polymers rises from 46.0% to 56.7%. Conversely, the average percentage of network structures declines from 54.0% to 43.3%. This observed phenomenon, where increased aqueous HCl content correlates with a higher percentage of cage structures, diverges from findings reported in the literature [46]. The discrepancy arises because the literature examines the reaction of $HSiCl_3$ in conjunction with methanol and water, while our study employs a direct mixture of TES and aqueous HCl, leading to differences in the extent and rate of hydrolysis and condensation. Fig. 2(i) and Table 1 show the ratios of the integrated areas of the Si–O–Si bands and the H–Si bands. The Si–O–Si/Si–H area ratio of HSQ polymers increases as the TES/H_2O volume ratio decreases, indicating a higher cross-linking density [46]. In the pyrolysis reaction, elevated cross-linking density results in a greater energetic barrier for the diffusion of silicon atoms within the matrix, leading to the formation of smaller SiQDs in the pyrolysis products [46,49]. Furthermore, the observation that increased aqueous HCl content cor-

Table 1
Synthesis conditions and FTIR analysis results of the TES-derived HSQ polymers.

Series	TES (mL)	H_2O (mL)	TES/ H_2O volume ratio	Network (%)	Cage (%)	Si–O–Si/H–Si
1	20	10	2.00	54.0 ± 0.9	46.0 ± 0.9	12.7 ± 0.6
2	20	20	1.00	52.5 ± 1.4	47.5 ± 1.4	13.9 ± 1.0
3	20	30	0.67	48.5 ± 1.5	51.5 ± 1.4	15.0 ± 0.4
4	20	40	0.50	43.3 ± 1.1	56.7 ± 1.1	16.4 ± 1.0

relates with a higher Si–O–Si/Si–H area ratio aligns with findings reported in the literature [46].

Fig. 3(a, b) shows the XRD patterns of the HSQ polymers and pyrolysis products. The broad diffraction peaks at ~23° in the HSQ polymers are associated with $HSiO_{1.5}$ [12]. The broad diffraction peaks at ~21° in the pyrolysis products are assigned to amorphous SiO_2 [12,46], and the diffraction peaks at 28°, 47°, and 56° correspond to the (111), (220), and (311) crystal planes of the crystalline silicon, respectively [12,46]. It can be seen that the HSQ polymers are converted from $HSiO_{1.5}$ to amorphous SiO_2 and crystalline silicon after the pyrolysis reaction. Moreover, the diffraction peaks of crystalline silicon in the series 4 pyrolysis product show weaker intensity and broader peak width, which may derive from smaller size or worse crystallinity. Following the methodology presented in the literature [46], we subtracted the amorphous SiO_2 component from the XRD patterns of the pyrolysis products, resulting in Fig. 3(c). Using the Scherrer equation [37], the dimensions of SiQDs within the matrix can be approximately estimated. To enhance the accuracy of the crystal size determination, a statistical analysis was conducted, as illustrated in Fig. 3(d). The average crystal sizes of SiQDs in the pyrolysis products for series 1–4 are 4.76 ± 0.46 nm, 4.30 ± 0.32 nm, 4.08 ± 0.44 nm, and 2.77 ± 0.37 nm, respectively. This gradual decrease in SiQD size is attributed to the higher cross-linking densities, which impede the diffusion and aggregation of silicon atoms.

Fig. 4(a, b) shows the Raman spectra of the HSQ polymers and pyrolysis products. It can be seen that the Raman characteristic peak of silicon located at 450–530 cm^{-1} is absent in the spectra of HSQ polymers. In contrast, the spectra of pyrolysis products show the existence of Raman peaks of silicon, which indicates that silicon is formed after the pyrolysis reaction. Fig. 4(c–f) presents enlarged views of the Raman spectra of pyrolysis products, specifically within the range of 400–600 cm^{-1}. According to existing literature [46,47,62], the Raman peak of silicon can be decomposed into two Gaussian peaks. Specifically, this is characterized by a broad peak approximately at 500 cm^{-1} and a sharp peak observed between 510 and 518 cm^{-1}, which correspond to the amorphous and crystalline silicon fractions, respectively. It is an effective method to evaluate the crystallinity of silicon using the crystalline fraction, which is obtained by calculating the integral area of silicon and amorphous silicon, as shown in the following equation [63]:

$$f_c = \frac{1}{1 + \gamma I_a^{\gamma}} \quad (1)$$

Where $I_a{}^{\gamma}$ represents the relative integrated intensity of the Raman band of amorphous silicon, which is equal to the integrated area of the amorphous part (I_a) divided by that of the crystalline part (I_c); γ represents the relative Raman cross-section, which is typically associated with the size of crystalline silicon [47,62–64]. Nevertheless, some researchers have employed a size-independent γ to calculate the crystalline fraction of SiQDs [46,65]. To facilitate a more effective comparison of the crystalline fractions of SiQDs with those reported in the literature, we utilized three different γ criteria, referred to as f_{c1} [64], f_{c2} [63], and f_{c3} [46], respectively. As illustrated in Fig. 4(c–f), all three crystalline fractions increase as the TES/H_2O volume ratio decreases. Notably, series 4 exhibits a crystalline fraction exceeding 90% across all three criteria, indicating its superior quality. Additionally, we examined the Raman spectra of octadecyl-passivated freestanding SiQDs derived from the pyrolysis products following etching and hydrosilylation, as shown in Fig. 4(g, h). Based on the trends observed in the py-

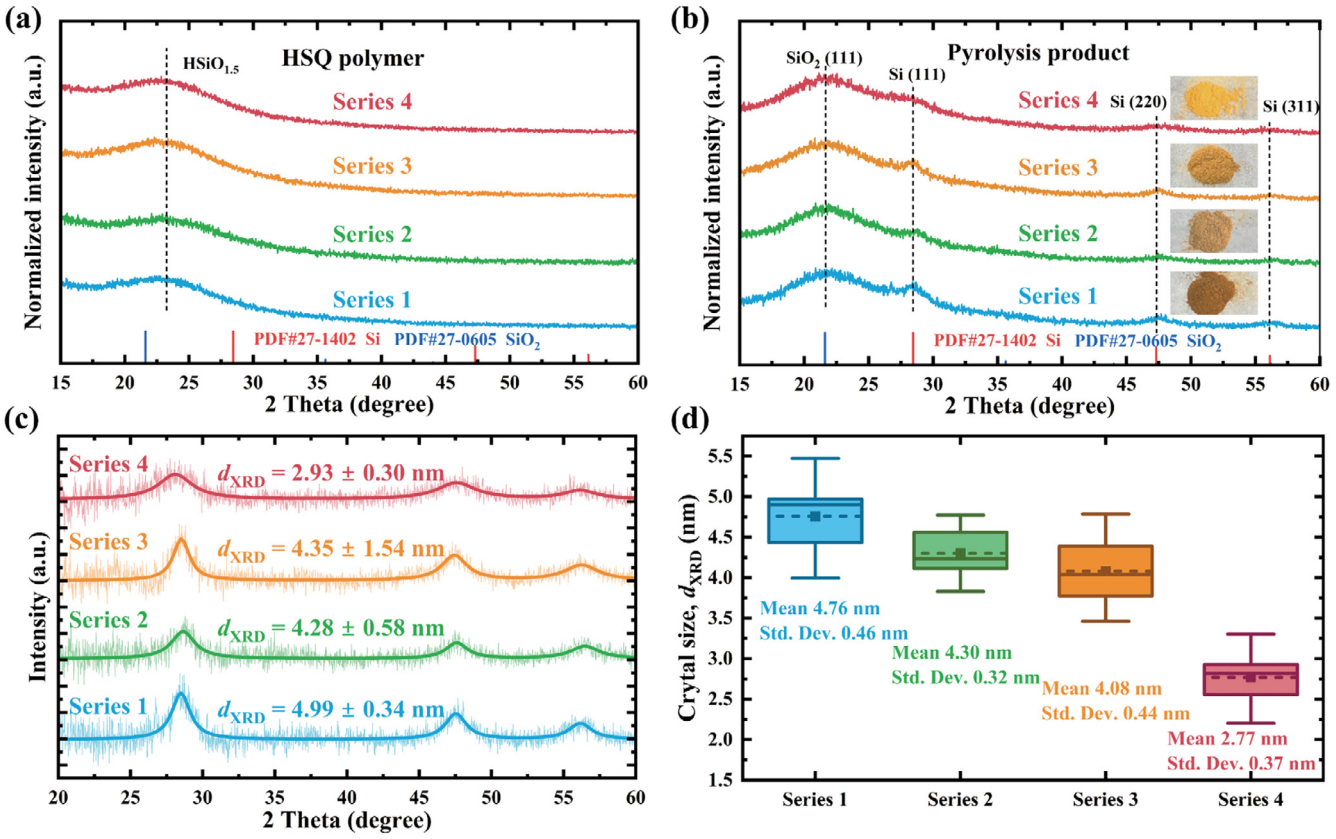

Fig. 3. (a, b) XRD patterns of HSQ polymers and pyrolysis products of series 1–4; (c) XRD patterns of the pyrolysis products with subtracted amorphous silica compositions (the light and dark red curves represent the raw data and the fitted curves, respectively. The crystal sizes of the SiQDs for series 1–4 were calculated using the Scherrer equation); (d) Box plots of crystal size of SiQDs in the pyrolysis products.

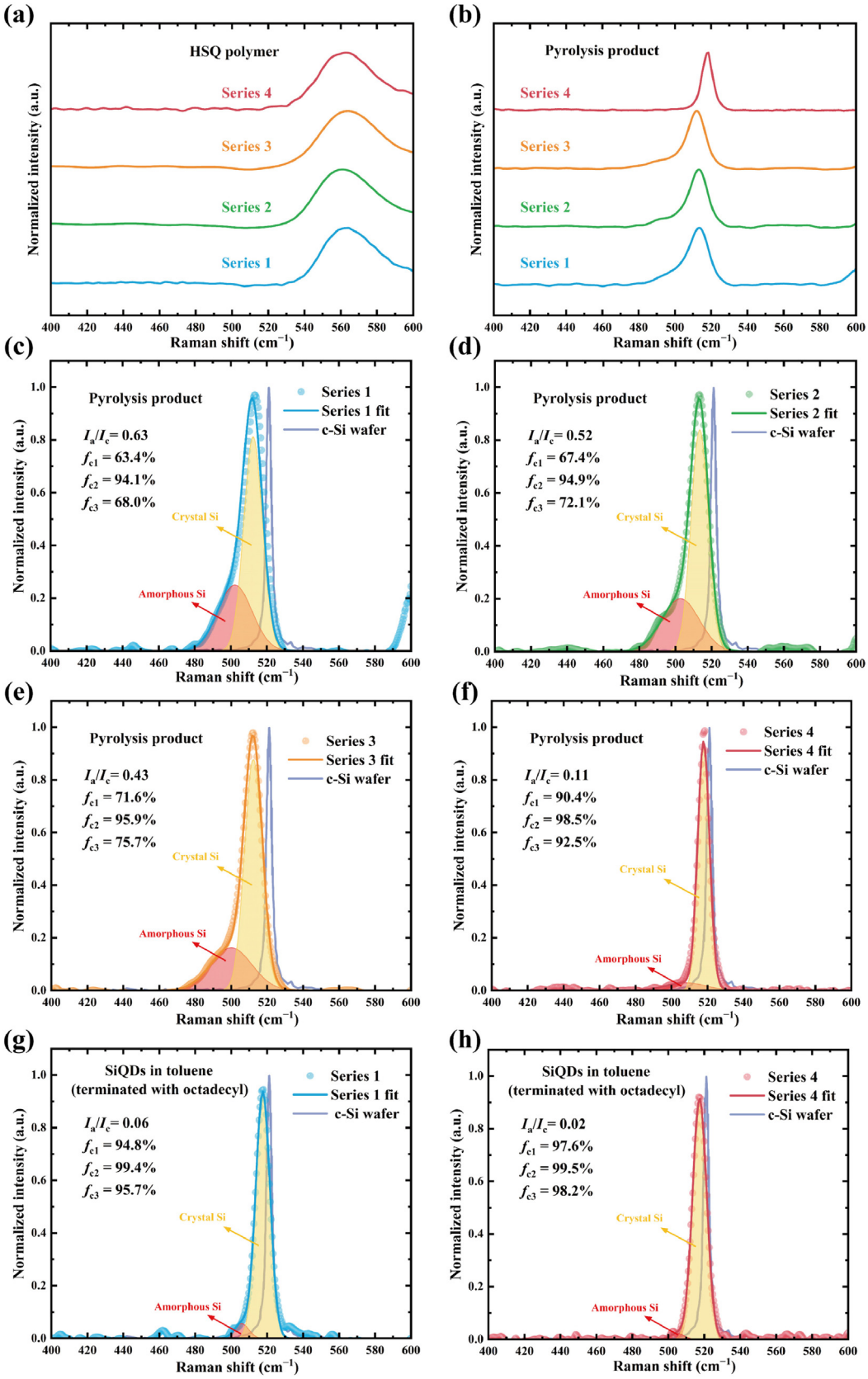

Fig. 4. (a, b) Raman spectra of HSQ polymers and pyrolysis products of series 1–4; (c–f) Enlarged views of the Raman spectra of the pyrolysis products; (g, h) Enlarged views of the Raman spectra of the octadecyl-passivated SiQDs in toluene.

Table 2
XRD and Raman analysis results of SiQDs in pyrolysis products/toluene.

Series	Crystal size, d_{XRD} (nm)	Relative Raman intensity, I_a/I_c	Crystalline fraction			ω_{Theo} (cm^{-1})	ω_{Exp} (cm^{-1})	Phonon induced $\Delta\omega$ (cm^{-1})	Stress-induced $\Delta\omega$ (cm^{-1})	Stress (GPa)
			f_{c1} (%)	f_{c2} (%)	f_{c3} (%)					
1	4.76 ± 0.46	0.66 ± 0.11 (0.056 ± 0.004)	62.1 ± 3.9 (95.0 ± 0.3)	93.7 ± 1.1 (99.4 ± 0.03)	66.9 ± 3.6 (95.9 ± 0.3)	518.9 ± 0.3	512.0 ± 1.3 (517.6 ± 0.1)	−2.1 ± 0.3	−6.8 ± 1.3 (−1.2 ± 0.3)	1.6 ± 0.3 (0.3 ± 0.1)
2	4.30 ± 0.32	0.57 ± 0.08	65.4 ± 3.2	94.4 ± 0.8	70.3 ± 2.9	518.6 ± 0.3	512.7 ± 2.3	−2.4 ± 0.3	−5.9 ± 2.6	1.4 ± 0.6
3	4.08 ± 0.44	0.38 ± 0.04	73.4 ± 1.9	95.9 ± 0.3	77.8 ± 1.9	518.3 ± 0.4	512.3 ± 0.9	−2.7 ± 0.4	−5.9 ± 0.9	1.4 ± 0.2
4	2.77 ± 0.37	0.10 ± 0.02 (0.031 ± 0.010)	90.7 ± 1.6 (97.0 ± 0.9)	98.4 ± 0.2 (99.5 ± 0.1)	92.9 ± 1.3 (97.7 ± 0.7)	515.9 ± 0.9	517.9 ± 1.1 (517.5 ± 0.1)	−5.1 ± 0.9	2.0 ± 1.8 (1.5 ± 0.9)	−0.5 ± 0.4 (−0.4 ± 0.2)

*The results for freestanding octadecyl-passivated SiQDs, which include only series 1 and series 4, are presented in parentheses.

rolysis products, only the most extreme series 1 and 4 were selected for comparison. The results demonstrate that the crystalline fraction of both series 1 and series 4 SiQDs is significantly higher compared to when they are embedded in a SiO_2 matrix, particularly for series 1. Veinot's group [66,67] has shown that the pristine SiQDs possess a core-shell structure, with an amorphous silicon shell surrounding a crystalline silicon core. This suggests that the amorphous silicon on the surface of the freestanding SiQDs, liberated from the SiO_2 matrix, is etched by HF during the etching process, resulting in the formation of dioxonium hexafluorosilicate [12]. Consequently, the higher crystalline fractions observed in the two series of octadecyl-passivated SiQDs can be attributed to the removal of amorphous silicon from the SiQD surface. Furthermore, it is noteworthy that series 4 passivated SiQDs exhibit a higher crystalline fraction compared to series 1 passivated SiQDs, which aligns with the trend observed in their pyrolysis counterparts, suggesting that the interior of series 4 SiQDs retains a greater crystalline character.

To assess reproducibility, the crystalline fractions of pyrolysis products from series 1 to 4 were statistically analyzed, as illustrated in Fig. 5(a–c) and Table 2. Notably, for all three γ-criteria [46,63,64], significant increases in the crystallinity of SiQDs in the pyrolysis products were observed with decreasing TES/H_2O volume ratios. To date, the highest recorded crystalline fraction (54%) of SiQDs in pyrolysis products was reported by Saitow's group [46]. As shown in Fig. 5(c), the crystalline fractions of SiQDs across the four series of pyrolysis products we prepared markedly exceeded this value. Furthermore, statistical analyses of the octadecyl-passivated SiQDs were conducted, as depicted in Fig. 5(d–f) and Table 2. It is clear that the crystalline fraction of series 4 consistently surpasses that of series 1, aligning with the trend in the pyrolysis products. Notably, to our knowledge, the highest crystalline fraction (92%) for freestanding SiQDs was also reported by Saitow et al. [47,62]. Fig. 5(e) indicates that the crystalline fractions of the freestanding SiQDs we prepared significantly exceed previously recorded values. However, as previously discussed, this high crystalline fraction primarily results from the removal of amorphous silicon from the surface of the SiQDs and does not accurately represent the degree of crystalline of the pristine SiQDs. Therefore, it is advisable to prioritize the crystalline fraction of SiQDs in the pyrolysis products, as it more reliably reflects the intrinsic crystallinity of the SiQDs.

In addition to the crystalline fraction, changes in the position of the Raman peak are noteworthy. Generally, the Raman peak position associated with phonon confinement for SiQDs is calculated using the following equation [47,68]:

$$\omega(d) = \omega_0 - A\left(\frac{a}{d}\right)^{\gamma} \tag{2}$$

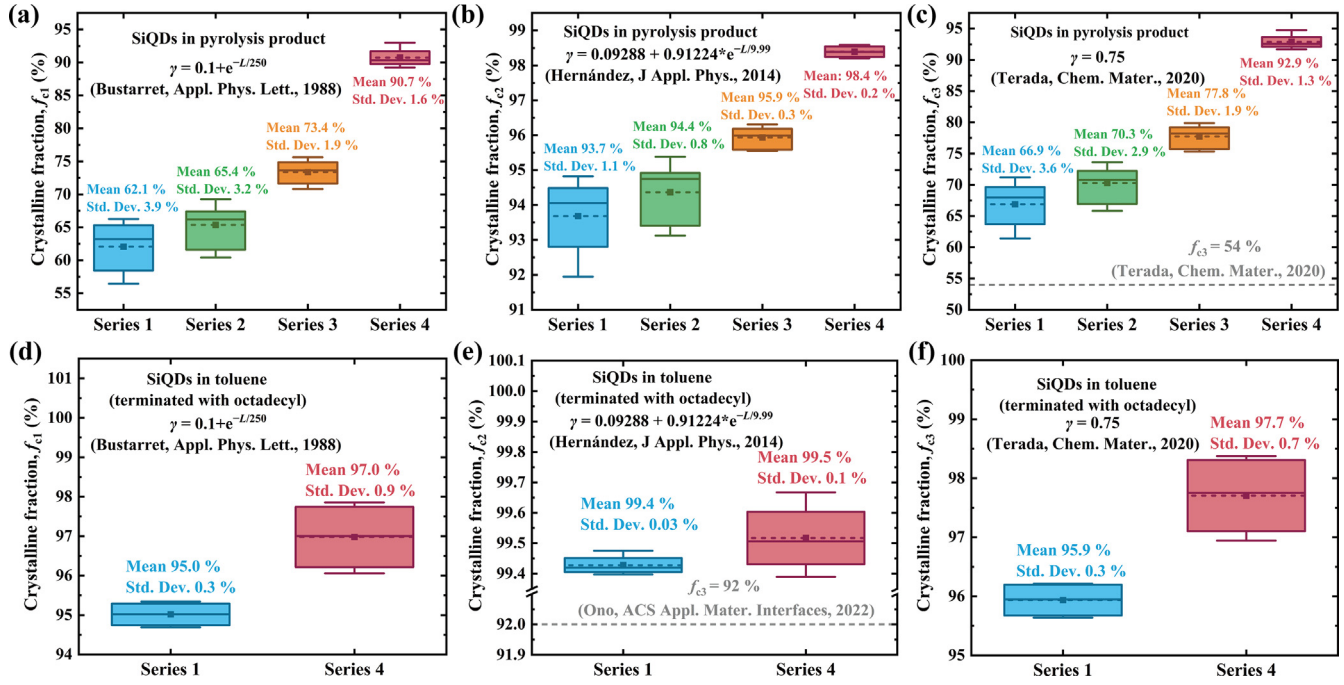

Fig. 5. (a–c) Box plots of crystalline fractions corresponding to the three γ-criteria for SiQDs in the pyrolysis products; (d–f) Box plots of crystalline fractions corresponding to the three γ-criteria for the octadecyl-passivated SiQDs in toluene.

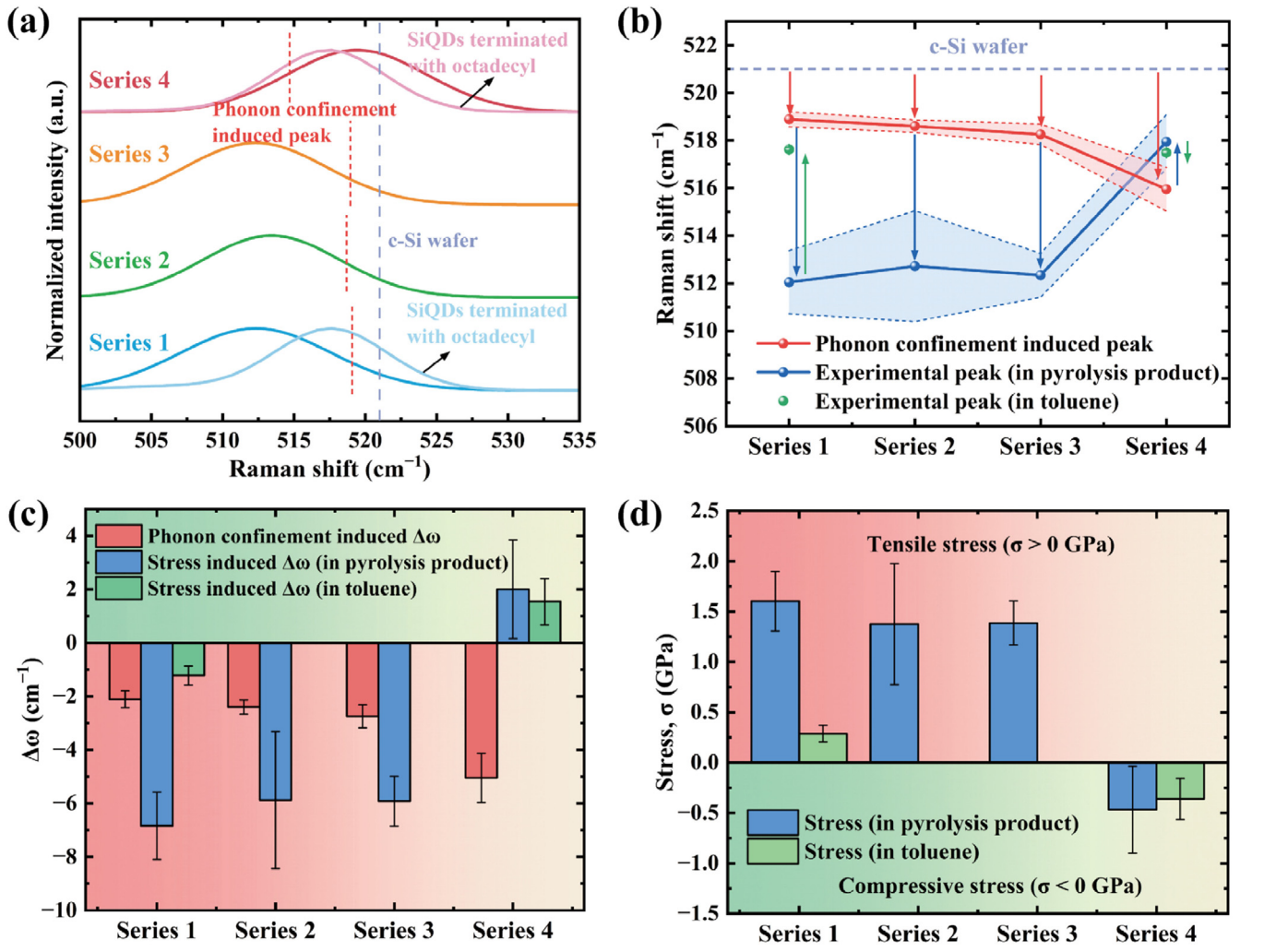

Fig. 6. (a) Crystalline silicon peaks of SiQDs. The blue-purple dashed line indicates the peak position of crystalline silicon wafer, and the red dashed line represents the peak position caused by phonon confinement effects; (b) Theoretical and experimental Raman shifts of the crystalline silicon peaks. The shaded areas represent the range of standard deviations; (c) Raman shift variations of the crystalline silicon peaks in SiQDs caused by phonon confinement effects and stress on SiQDs; (d) Stress existed on SiQDs. Positive and negative stresses indicate tensile and compressive stresses, corresponding to the red-white and green-white regions, respectively.

Where ω_n represents the Raman peak position of bulk silicon (521 cm^{-1}), A and γ are constants defining phonon confinement (47.41 and 1.44, respectively), a denotes the lattice constant of crystalline silicon (0.543 nm), and d signifies the diameter of SiQDs (in nm) [47,68]. By substituting the crystal sizes of SiQDs, calculated via the aforementioned Scherrer equation, into Eq. (2), the peak positions of phonon confinement-induced SiQDs can be determined. Consequently, the theoretical and experimental Raman peak positions of crystalline silicon are illustrated in Fig. 6(a). Furthermore, the peak positions underwent statistical analysis, with the error bars and the area enclosed by the dashed line representing the range of one standard deviation. As shown in Fig. 6(b) and Table 2, the peak positions corresponding to phonon confinement for series 1–4 SiQDs are, in order, 518.9 ± 0.3 cm^{-1}, 518.6 ± 0.3 cm^{-1}, 518.3 ± 0.4 cm^{-1}, and 515.9 ± 0.9 cm^{-1}. In contrast, the peak positions of SiQDs in pyrolysis products are 512.0 ± 1.3 cm^{-1}, 512.7 ± 2.3 cm^{-1}, 512.3 ± 0.9 cm^{-1}, and 517.9 ± 1.1 cm^{-1}. The Raman peak positions of the freestanding SiQDs in toluene are 517.6 ± 0.1 cm^{-1} (series 1) and 517.5 ± 0.1 cm^{-1} (series 4). It is evident that, relative to the theoretical values, the experimental values exhibit significant redshifts or blueshifts, as demonstrated in Fig. 6(c) and Table 2. According to previous studies, this shift arises from the stresses that existed on the SiQDs, which can be calculated as follows [47]:

$$\Delta\omega = -\kappa\sigma \tag{3}$$

Where $\Delta\omega$ represents the shift value (changed ω minus initial ω) of the Raman peak under ambient pressure, κ is the wave number stress factor (4.27 for SiQDs) [47], and the positive and negative values of the stress correspond to tensile and compressive stresses, respectively. The calculated stresses on the SiQDs are presented in Fig. 6(d) and Table 2. The Raman peak positions of crystalline silicon for series 1–3 pyrolysis products exhibit a significant redshift relative to theoretical values, attributed to the tensile stress imposed on the SiQDs by the siloxane network on their surfaces [58]. Conversely, the crystalline silicon Raman peak positions of series 4 pyrolysis products show a notable blueshift relative to theoretical values, resulting from an increase in compression induced by the SiO_2 matrix due to the reduction in SiQD size [63]. Studies indicate that this matrix-induced compressive stress is 0 GPa when the crystal size of the nanocrystalline silicon within the matrix is greater than or equal to 4 nm [63]. In contrast, when the crystal size is smaller than 4 nm, the compressive stress significantly increases with size reduction. Given that the crystal sizes of series 1–3 pyrolysis products are all larger than 4 nm, they should not experience compressive stress. For the SiQDs in series 4 pyrolysis

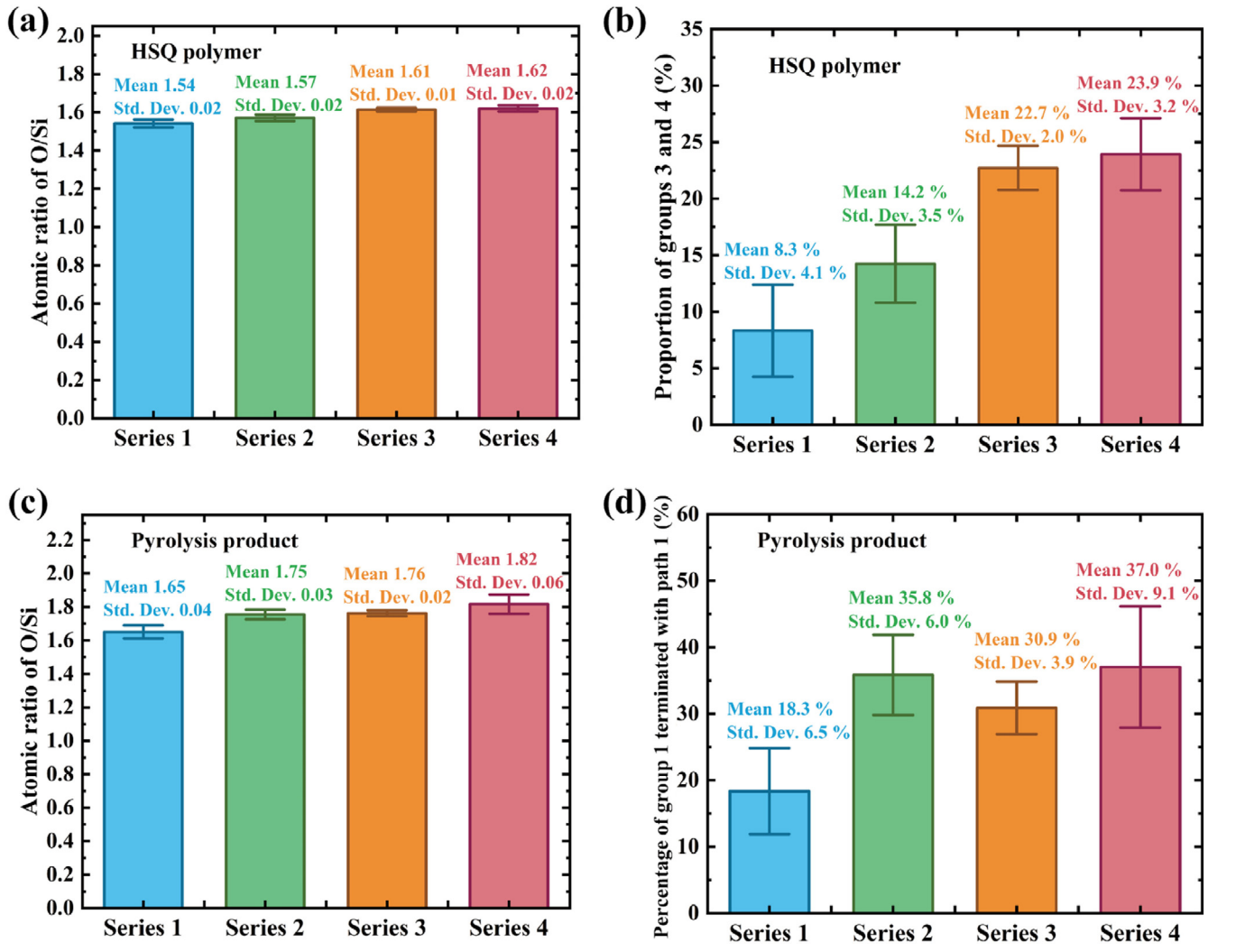

Fig. 7. (a) Atomic ratio of O to Si for the HSQ polymers; (b) Proportion of groups 3 and 4 in the HSQ polymers; (c) Atomic ratio of O to Si for the pyrolysis products; (d) Proportion of group 1 terminated with path 1.

products, which have an average crystal size of 2.77 ± 0.37 nm, the calculated average stress is −0.47 GPa, comparable to the compressive stress experienced by nanocrystalline silica matrices with a size of 2.6 nm in the literature (−0.3 GPa) [63]. Additionally, the Raman peak position of crystalline silicon for series 1 freestanding SiQDs in toluene exhibits a small redshift relative to the theoretical value but a significant blueshift compared to its pyrolytic counterpart. This shift is attributed to the removal of the siloxane network during the etching process, although tensile stresses remain due to the presence of octadecyl groups. The Raman peak position of crystalline Si for series 4 reveals a small blueshift relative to the theoretical value but a redshift compared to its pyrolytic counterpart, attributed to the tensile stress from the octadecyl group. Notably, the compressive stress generated by the SiO_2 matrix persists even after removal by HF, suggesting that this compression induces irreversible changes in the Si–Si bonds. Furthermore, the retention of compressive stress helps prevent the amorphization of the SiQD surfaces caused by the tensile stress of the ligand by counteracting part of the effects of this tensile stress.

Figs. S1 and S2 in Supplementary materials present the high-resolution XPS Si 2p spectra of the HSQ polymer and the pyrolysis products. Notably, the intensity of the Si^{0+} sub-peak in series 4 pyrolysis product is significantly weaker than that of series 1–3, which may be attributed to the smaller size of series 4 SiQDs, resulting in a higher surface-to-volume ratio [1]. Fig. 7(a, c) illustrates the atomic ratio of O to Si for the HSQ polymers and pyrolysis products, derived from the Si 2p and O 1s spectra shown in Figs. S1 and S2. It is important to note that the error bars represent a range of standard deviations. For HSQ polymers, a composition with an O/Si ratio of 1.5 indicates the presence of exclusive groups 1−2. An O/Si ratio of 2 signifies a composition comprising solely groups 3–4. Given that the O/Si ratios for series 1 through 4 HSQ polymers range from 1.54 to 1.62, it follows that none of these polymers consist solely of groups 1–2 or 3–4. Instead, they contain a combination of groups 1–4 (i.e., $[HSiO_{1.5}]_a[HSiO_{1.5}(C_2H_5)_n]_b[SiO_2]_c[SiO_2(C_2H_5)_m]_d$). Therefore, the O/Si ratio can be utilized to determine the proportion of groups 3–4 in HSQ polymers, as illustrated in Fig. 7(b) and Table 3. The average percentage of groups 3–4 in the HSQ polymers increases from 8.3% to 23.9% as the TES/H_2O volume ratio decreases, indicating an increase in cross-linking density. This finding further corroborates the observation that HSQ polymers synthesized at lower TES/H_2O volume ratios exhibit higher cross-linking densities, as determined by FTIR spectra. The successive reaction of the pyrolysis process is shown below:

$$4HSiO_{1.5} \overset{\text{Path 1}}{\rightarrow} SiH_4 \uparrow + 3SiO_2 \overset{\text{Path 2}}{\rightarrow} Si + 3SiO_2 + 2H_2 \uparrow \quad (4)$$

If $HSiO_{1.5}$ (i.e., group 1) had only terminated the reaction in path 2, SiO_2 and Si would be formed, and the O/Si ratios of the

Table 3
XPS analysis results of HSQ polymers and pyrolysis products.

Series	O/Si ratio in HSQ polymers	Proportion of groups 3–4 in HSQ polymers (%)	O/Si ratio in pyrolysis products	Proportion of group 1 terminated with path 1 (%)
1	1.54 ± 0.02	8.3 ± 4.1	1.65 ± 0.04	18.3 ± 6.5
2	1.57 ± 0.02	14.2 ± 3.5	1.75 ± 0.03	35.8 ± 6.0
3	1.61 ± 0.01	22.7 ± 2.0	1.76 ± 0.02	30.9 ± 3.9
4	1.62 ± 0.02	23.9 ± 3.2	1.82 ± 0.06	37.0 ± 9.1

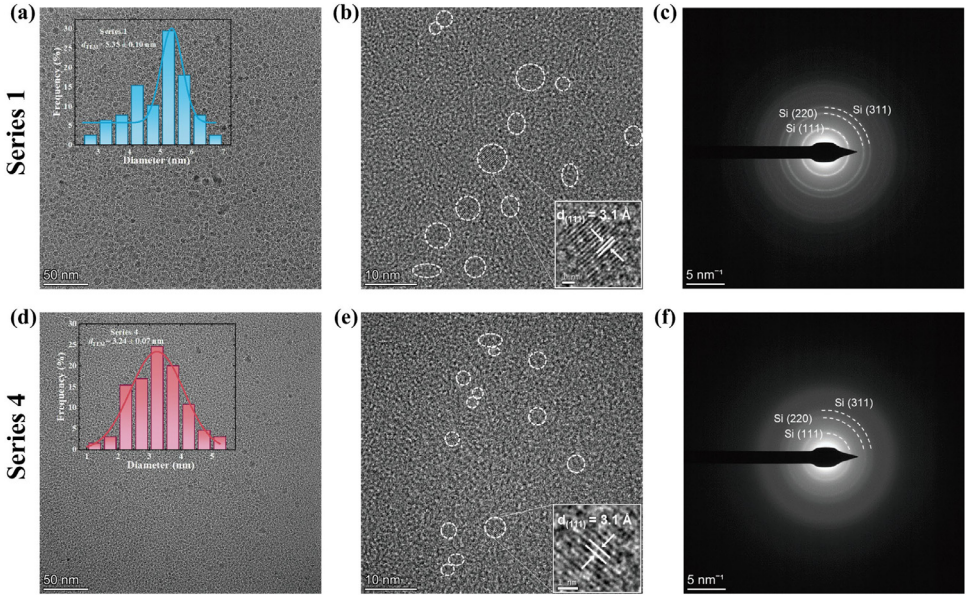

Fig. 8. (a–c) TEM image, HR-TEM image, and SAED pattern of the series 1 SiQDs; (d–f) TEM image, HR-TEM image, and SAED pattern of the series 4 SiQDs.

pyrolysis products should be the same (O/Si = 1.5) as it was before pyrolysis. However, the O/Si ratios of the pyrolysis products increased with respect to the HSQ polymers, implying that partial $HSiO_{1.5}$ takes path 1 as the reaction termination. This is because when this path is taken as the reaction termination, the decomposed SiH_4 escapes from the matrix (O/Si = 2 in pyrolysis products) rather than decomposing into Si and H_2 (O/Si = 1.5 in pyrolysis products), which finally leads to increases in the O/Si ratios. Therefore, the increases in the percentages of O/Si = 2 for the pyrolysis products with respect to their HSQ polymers are contributed only by the portion of the HSQ polymers in which group 1 terminates in path 1. As shown in Fig. 7(d) and Table 3, the average percentages of O/Si = 2 for series 1–4 pyrolysis products are increased by 18.3%, 35.8%, 30.9%, and 37.0% compared to series 1–4 HSQ polymers, indicating that a higher percentage of group 1 in series 4 terminates the reaction in path 1. This is because the higher cross-linking density in series 4 hinders the diffusion of silicon atoms and thus prevents them from aggregating to form SiQDs [46,49,52]. The undiffused silicon atoms return to SH_4 form by combining with H_2 and eventually escape from the matrix. In other words, the escape of SiH_4 (terminated with path 1) and the diffusion of Si atoms (terminated with path 2) are competitive processes. The former leads to a size decrease of SiQDs, while the latter leads to a size increase of SiQDs. Therefore, we conclude that large/small cross-link density makes the pyrolysis of group 1 more likely to terminate with path 1/2.

To optimize labor and resource utilization, subsequent characterizations, including TEM and PL, were conducted exclusively on the two most representative extremes: series 1 and series 4. Fig. 8(a, d) presents the TEM images of series 1 and series 4 SiQDs, along with the corresponding frequency distributions of SiQD sizes. The average sizes were observed to be 5.35 ± 0.10 nm for series 1 and 3.24 ± 0.07 nm for series 4. The significantly smaller size of series 4 SiQDs compared to series 1 supports the predictions regarding SiQD sizes derived from the FTIR, XRD, and XPS analyses previously described. Furthermore, the average sizes of SiQDs obtained from TEM images are slightly larger than those derived from XRD patterns, with series 1 measuring 4.76 ± 0.46 nm and series 4 measuring 2.77 ± 0.37 nm. This discrepancy is attributed to the presence of ligands, dangling bonds, and silicon oxide on the surfaces of freestanding SiQDs [47,62], as well as the fact that the Scherrer equation does not account for stress effects [46,69,70], which together result in a larger average size of SiQDs derived from TEM compared to those derived from XRD experiments. HR-TEM images of the series 1 and series 4 SiQDs are shown in Fig. 8(b, e), where the white dash circles highlight the SiQDs. The inset shows localized zoom-in of the corresponding SiQDs, and the lattice fringes can be easily observed. The lattice spacings of the series 1 and series 4 SiQDs both are 0.31 nm, in line with the *d*-spacing of the (111) plane of the diamond cubic lattice of silicon [13]. Fig. 8(c, f) shows the SAED patterns of SiQDs with the selected areas taken from the TEM images of Fig. 8(a, d). The SAED patterns show three diffraction rings corresponding to the (111), (220), and (311) planes of the diamond cubic crystalline of silicon, which is consistent with the analysis of the XRD patterns. The SAED patterns show typical polycrystalline characteristics, which aligns with the literature [13,71]. The diffraction rings of series 4 are weaker than those of series 1, which can be attributed to the lower proportion of series 1 SiQDs within the electron diffraction area, rather than a lower crystallinity of series 4 relative to series 1. This interpretation is supported by the XRD and Raman results discussed above.

Fig. 9(a, b) shows the two-dimensional PL spectra of the series 1 and 4 SiQDs, where the *x*-axis, *y*-axis, and *z*-axis represent

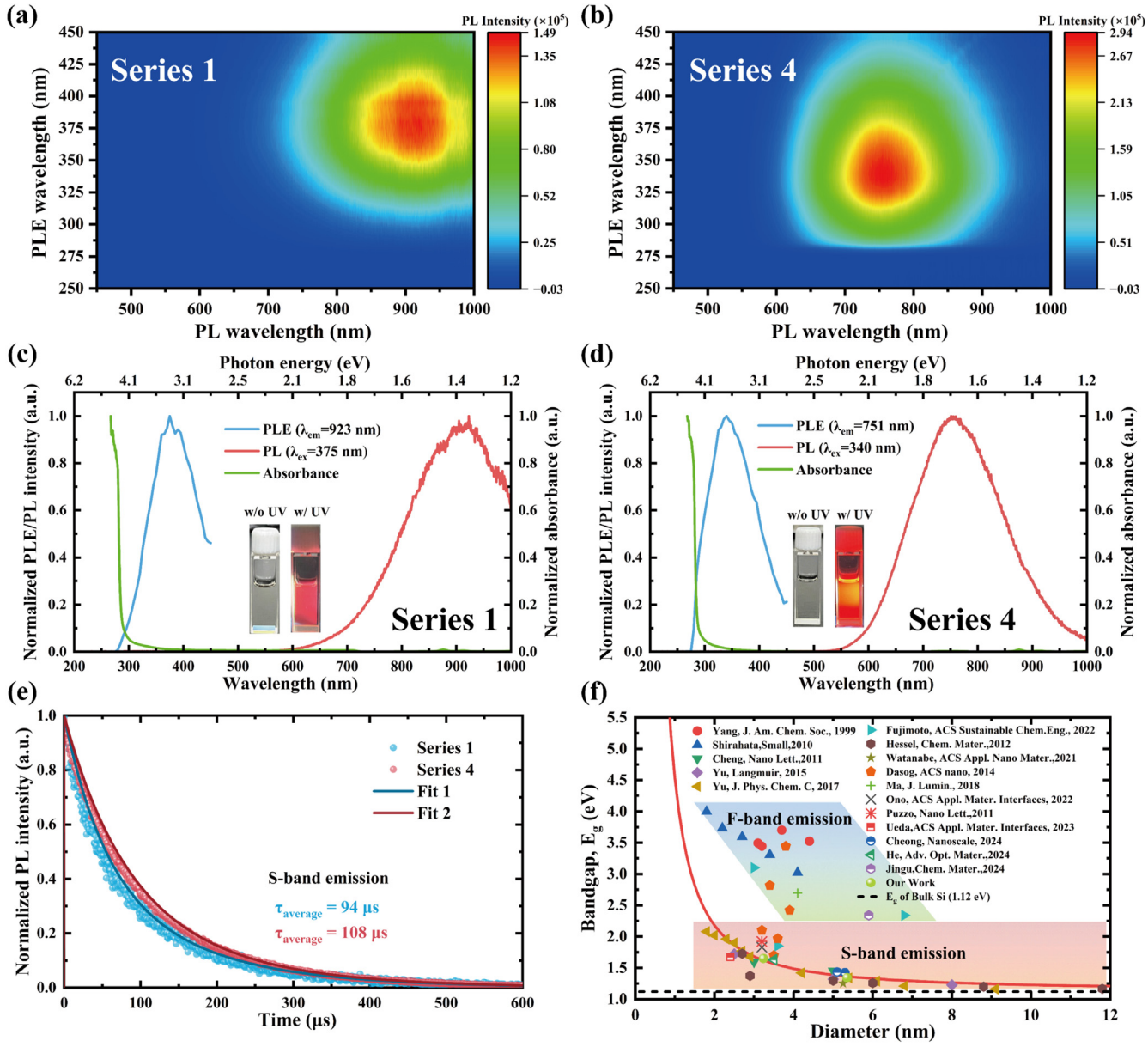

Fig. 9. (a, b) Two-dimensional PL spectra of SiQDs of series 1 and 4; (c, d) PLE, PL, UV–Vis absorption spectra of SiQDs of series 1 and 4. The insets show photographs of SiQDs of series 1 and 4 under ambient light and UV light of 365 nm; (e) PL decay profiles for SiQDs of series 1 and 4 (λ_{ex} = 355 nm, λ_{em} = 750 nm); (f) Relationship between the size and bandgap energy of SiQDs in our work and in the previous literature. The red curve represents the function of the EMA method.

the emission wavelength, excitation wavelength, and PL intensity, respectively. Significant differences can be seen between the two spectra. The PL and PLE peak wavelengths of series 4 are significantly blue-shifted compared to those of series 1, suggesting that the size of the SiQDs in series 4 is much smaller than that in series 1. This observation aligns with the reduced size indicated by the XRD patterns and TEM images. Specifically, we compared the PL, PLE, and UV–Vis absorption spectra of series 1 and series 4 SiQDs, as illustrated in Fig. 9(c, d). The insets in these figures display optical photographs of diluted colloidal SiQDs under ambient and UV light (365 nm) irradiation. Series 4 appears noticeably redder and brighter under UV light, which can be attributed to higher PL components in the visible red spectrum and possibly a greater PLQY, a topic that will be addressed subsequently. The PL maxima for series 1 and series 4 are located at 923 nm (1.34 eV) and 751 nm (1.65 eV), respectively; this significant blueshift is ascribed to the widening of the Γ–*X* indirect bandgap caused by the size reduction of the SiQDs [3,72]. Additionally, the PLE maxima for series 1 and series 4 occur at 375 nm (3.31 eV) and 340 nm (3.65 eV), respectively, with these blueshifts linked to the widening of the Γ–Γ direct bandgap due to the decrease in SiQD size [3,73]. Notably, as size decreases, the Γ–Γ direct bandgap transitions from 3.32 eV (bulk Si, > 10 nm) to 3.31 eV (series 1, ~5 nm) and to 3.65 eV (series 4, ~3 nm). This observed trend of the Γ-valley bandgap first redshifting and then blueshifting is a consequence of quantum confinement at the nanoscale, as confirmed by experimental and theoretical investigations conducted by de Boer et al. [74] and Luo et al. [73]. Furthermore, the UV–Vis absorption spectra of series 1 and series 4 SiQDs are consistent with the trends observed in their respective PLE spectra, displaying minimal absorption in the 400–1000 nm range but a marked increase in absorption below 400 nm. The decay time analyses of the series 1 and 4 SiQDs are shown in Fig. 9(e). The decay data are fitted by double-exponential function, and the corresponding average PL

decay lifetimes are 94 and 108 μs, which are comparable to the lifetimes reported in the literature [1,47,58]. The microsecond-level lifetimes provide decisive evidence that the emissions of the series 1 and 4 cases both belong to the S-band emissions [75]. Furthermore, as illustrated in Fig. 9(a, b), there is no evident excitation wavelength dependence observed for both series 1 and series 4 SiQDs. This finding provides additional evidence that the PL in this context corresponds exclusively to S-band emissions rather than F-band emissions. Fig. 9(f) shows the relationship between the size and bandgap energy of SiQDs in our work and in the previous literature [7,9,16,37,39,41,47,58,59,62,67,76–80], where the red line is the fitted curve of the effective mass approximation (EMA) method [10], and the black dashed line represents the bandgap of bulk silicon (1.12 eV). Our results are very close to the EMA curve, confirming that the prepared SiQDs belong to the S-band emission once again. Additionally, the blue-green region indicates SiQDs exhibiting F-band emission, while the red-orange region indicates SiQDs exhibiting S-band emission.

To better understand the PL properties of the prepared SiQDs from the two series, a statistical analysis of the relevant PL parameters is essential. Due to the limitations of the PL spectrometer, which captures spectra only up to 1000 nm (with a PLE wavelength of 330 nm), Gaussian functions were employed to fit the PL spectra, thereby restoring the complete profiles, as illustrated in Fig. 10(a). All subsequent statistics and comparisons of PL parameters are based on these fitted curves. As shown in Fig. 10(b), the mean PL center wavelength for series 4 is observed at 764.1 nm, representing a blueshift of 114.9 nm compared to series 1 (879.0 nm), which is attributed to the reduced size of the SiQDs. Fig. 10(c) presents the full width at half maximum (FWHM) of the PL peaks for series 1 and series 4 SiQDs. Series 4 exhibits a smaller mean FWHM, indicating a more homogenous particle size distribution and reflecting the superior quality of these SiQDs [41,57]. Regarding PLQY, the spectrometer supports measurements up to 800 nm, which can be extended to 850 nm with appropriate correction methods; however, this range is insufficient to accurately evaluate series 1 and series 4, particularly series 1. Consequently, the absolute PLQY obtained from direct measurements is limited to wavelengths up to 850 nm and does not accurately represent the PLQY over the entire spectrum. Therefore, it is imperative to reconstruct the PLQY across the full spectrum to enable a fair comparison between the PLQYs of series 1 and series 4. The calculation equation of absolute PLQY is shown below [15,81]:

$$\mathrm{PLQY} = \frac{N_{\mathrm{PhotonsEmitted}}}{N_{\mathrm{PhotonsAbsorbed}}} = \frac{I_{\mathrm{PL,sample}} - I_{\mathrm{PL,blank}}}{I_{\mathrm{PLE,blank}} - I_{\mathrm{PLE,sample}}} \tag{5}$$

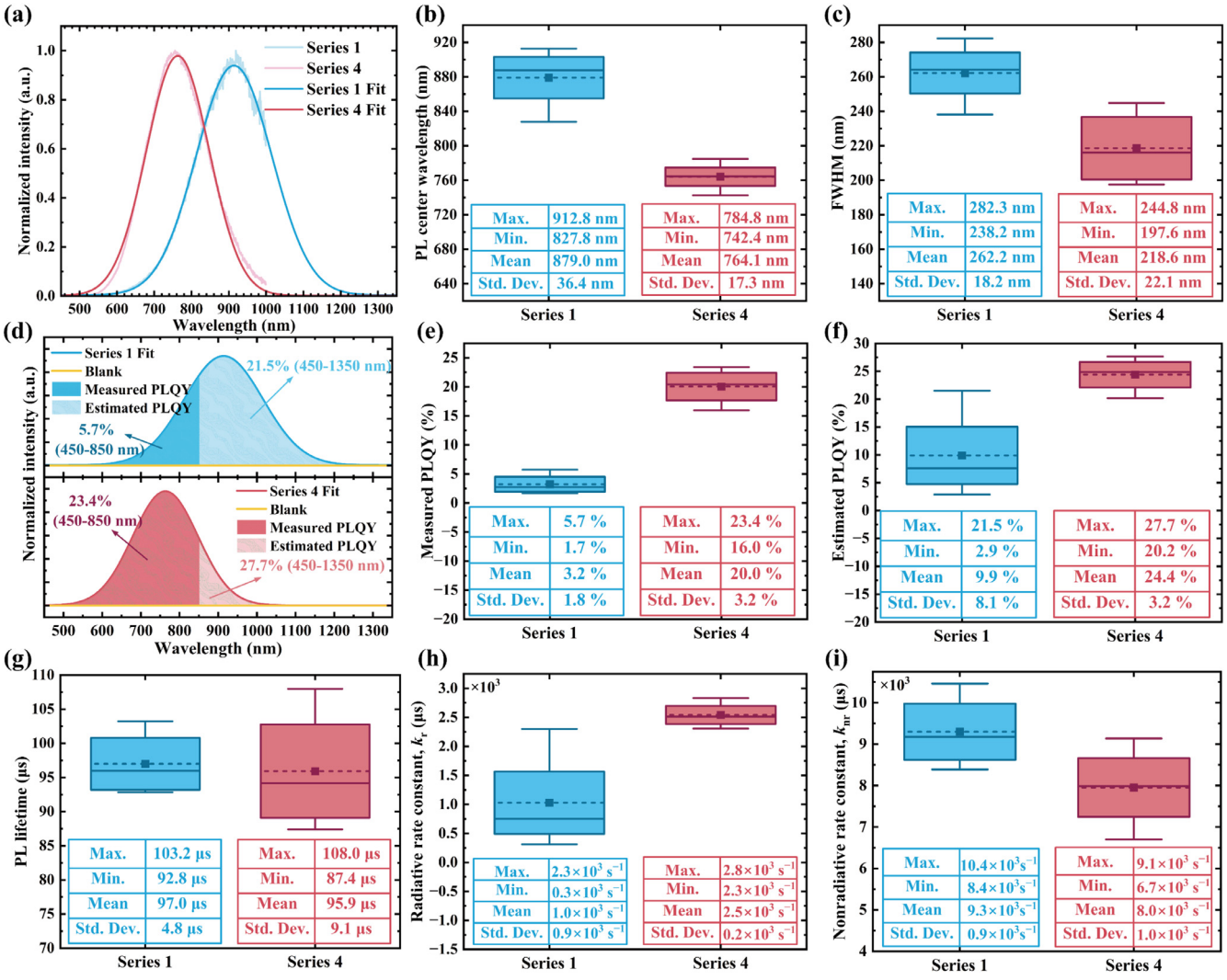

Fig. 10. (a) Normalized PL spectra of series 1 and 4 with fitted curves; (b, c) Box plots of the PL peak wavelength and FWHM for SiQDs of series 1 and 4; (d) Correlation between the PLQY and the integrated PL spectral intensity for SiQDs in series 1 and 4; (e, f) Box plots of the measured PLQY and the estimated PLQY for SiQDs of series 1 and 4; (g–i) Box plots of the PL lifetime, k_n, and k_{nr} for SiQDs of series 1 and 4.

Where I_{PL} is the integrated PL intensity, and I_{PLE} is the integrated PLE intensity. The measured champion PLQYs for series 1 and series 4 are 5.7% and 23.4%, respectively, and these values were used to demonstrate the recovery of the PLQYs of the full spectra. By substituting the integrated area of the measured spectrum ($I_{PL,\ sample}$) and the measured PLQYs into Eq. (5), the estimated PLQYs for the full spectra of series 1 and series 4 SiQDs were determined to be 21.5% and 27.7%, respectively, as shown in Fig. 10(d). Fig. 10(e, f) presents box plots of the measured and estimated PLQYs for series 1 and series 4 SiQDs. The mean measured PLQY for series 1 SiQDs is 3.2%, while the estimated PLQY is 9.9%. In contrast, series 4 SiQDs exhibit mean measured and estimated PLQYs of 20.0% and 24.4%, respectively. The significantly higher PLQY for series 4 compared to series 1 can be attributed to its greater crystalline fraction [1]. Nevertheless, the obtained PLQY of ~25% (in toluene) remains substantially lower than the current highest PLQY of ~80% (in toluene) reported by Saitow's group [47,59], which is primarily due to the unoptimized surface functionalization and purification processes that severely limit the PLQY [82,83]. Fig. 10(g) presents the box plots of PL lifetimes for series 1 and series 4 SiQDs. The results indicate no significant difference between the PL lifetimes of the two series of SiQDs. Furthermore, the radiative and nonradiative recombination rate constants (k_r, k_{nr}) can be obtained from τ and PLQY by the following equation [1,47]:

$$\mathrm{PLQY} = \frac{k_r}{k_r + k_{nr}} = k_r \tau \tag{6}$$

Where k_r and k_{nr} are the radiative and non-radiative rate constants of photo-excited electron-hole pairs, τ is the average PL decay lifetime. Hence, the interband recombination process between the electrons in the conduction band and the holes in the valence band of the SiQDs can be analyzed, as shown in Fig. 10(h, i). The k_r for series 4 is 1500 s^{-1} higher than that of series 1, whereas the k_{nr} for series 4 is 1300 s^{-1} lower than that of series 1. This observation can primarily be attributed to a higher crystalline fraction of series 4, which directly influences the recombination dynamics. Specifically, the increased silicon crystalline fraction in series 4 enhances radiative recombination by providing additional radiative recombination centers with enhanced efficiency, while reducing the impact of amorphous regions, which serve as nonradiative recombination centers [1,56]. The PL parameters of series 1 and series 4 SiQDs are summarized in Table 4.

It is noteworthy that although the crystalline fractions of the SiQDs in series 1 and series 4 differ considerably within the SiO_2 matrix, this difference in crystalline fraction narrows to within 2% following HF etching and hydrosilylation. Despite the fact that the PLQY of the series 4 is significantly higher than that of series 1—an observation that may appear paradoxical at first glance—we hypothesize that amorphous components are present not only on the surface but also within the SiQDs. The core region serves as the primary site for radiative recombination, and amorphous components located near the core exert a stronger suppressive effect on radiative recombination compared to those situated nearer the surface. Consequently, although the crystalline fraction of both series 1 and series 4 exceeds 95% after etching, series 4 contains a higher proportion of crystalline components concentrated near the SiQD core. This distribution leads to a significantly accelerated radiative recombination rate of series 4 relative to series 1, while the nonradiative recombination rate of series 4 is slower compared to that of series 1. Given that conventional Raman characterization cannot resolve the distribution of amorphous components in SiQDs smaller than 10 nm, this hypothesis explains the observed relationship between PLQY and crystalline fraction. Furthermore, smaller SiQDs tend to have larger surface-to-volume ratios, wherein (1) the effects of surface dangling bonds, oxides, and other defects on radiative recombination are more pronounced [47], and (2) the high-frequency vibrational modes of the organic ligands dominate, exacerbating nonradiative relaxation [1]. Therefore, smaller sizes imply the presence of more nonradiative recombination centers at the surface. Nevertheless, series 4 SiQDs (~3 nm) exhibit significantly higher PLQY compared to series 1 SiQDs (~5 nm), further indicating that the increased number of crystalline components within the SiQDs compensates for potential losses in radiative recombination due to the reduced size. Overall, the higher PLQY obtained for series 4 is attributed to the higher crystalline fraction. A comparison of PL properties of small SiQDs synthesized using pyrolysis of HSQ polymer in the literature is shown in Table 5. As can be seen our work obtained the highest crystalline fraction (~100%) up to date.

By integrating FTIR, XRD, Raman, XPS, TEM, and PL analyses, we conclude that the reaction process for the formation of SiQDs is illustrated in Fig. 11. At a low volume of aqueous HCl (series 1), inadequate hydrolysis results in a decrease in groups 1 and 3 and an increase in groups 2 and 4 within the HSQ polymer. This situation leads to a lower percentage of cage structures and a corresponding higher percentage of network structures. It is noted that the network structure is characterized by a higher number of ethoxy groups and fewer siloxane crossings. Methoxy groups have been reported to facilitate the "opening up" of the siloxane network in HSQ polymers [46,49], thereby reducing the cross-linking density; this also holds true for ethoxy groups. Similarly, ethoxy groups, due to their longer chain compared to methoxy groups, are likely to "opening up" the siloxane network to an even greater extent. Consequently, the network structure exhibits a relatively low cross-linking density, which results in a high diffusion density of silicon atoms, promoting the formation of large SiQDs. Furthermore, the diverse opening mechanisms of different groups result in significant non-uniformity in the diffusion barriers, leading to variable diffusion rates of silicon atoms. Therefore, the high quantities of groups 2 and 4 result in low diffusion uniformity. We posit that the inhomogeneous diffusion of silicon atoms is primarily responsible for the formation of amorphous silicon. Notably, the amorphous silicon formed is present not only on the surfaces of SiQDs but also in small amounts within them. As the volume of aqueous HCl increases (series 2 and 3), hydrolysis becomes increasingly effective, resulting in a higher number of groups 1 and 3 and a lower number of groups 2 and 4 within the HSQ polymer. This transition results in an increased proportion of cage structures and a corresponding decrease in the proportion of network structures. Additionally, there is a reduction in ethoxy groups and an increase in siloxane cross-linking in the network structure, leading to a moderate cross-linking density and moderate diffusion uniformity. Consequently, SiQDs of medium size and crystallinity are formed. It is important to note that the increase in cross-linking density makes silicon atoms that fail to diffuse more likely to recombine with hydrogen to form SiH_4 and escape from the matrix. Ultimately, when the concentration of aqueous HCl reaches a threshold (series 4),

Table 4
PL results for SiQDs of series 1 and series 4.

Series	TEM size, d_{TEM} (nm)	PL center (nm)	FWHM (nm)	Measured PLQY (%)	Estimated PLQY (%)	PL lifetime (μs)	k_r (s^{-1})	k_{nr} (s^{-1})
1	3.24±0.07	879.0±36.4	262.2±18.2	3.2±1.8	9.9±8.1	97.0±4.8	1000±900	9300±900
4	5.35±0.10	764.1±17.3	218.6±22.1	20.0±3.2	24.4±3.2	95.9±9.1	2500±200	8000±1000

Table 5
Comparison of small SiQDs synthesized using HSQ polymer pyrolysis.

Year	Precursor	Size (nm)	Relative Raman intensity	Crystalline Fraction, f_{c1}, f_{c2}, f_{c3} (%)			Ligand	PL peak (nm)	PLQY (%)	Refs.
2017	Trichlorosilane	0.8	–	–	–	–	Dodecyl	~450	3	[52]
2019	Triethoxysilane	1.8	–	–	–	–	Decyl	617	8	[84]
2020	Trichlorosilane	3.6	1.33	43.8	86.5	50	Dodecyl	~740	25	[46]
2021	Triethoxysilane	2.2	–	–	–	–	Undecenoic acid	630	19	[85]
2022	HSQ	3.2	0.49*	67.6*	92*	73.1*	Decyl	667	54	[47]
2024	Trichlorosilane	2.4	0.62*	61.5*	90*	68.3*	Decyl	740	77	[59]
2024	Triethoxysilane	3.24	0.10	90.7	98.4	92.9	Octadecyl	764.1	24.4	This study
			0.03*	97.0*	99.5*	97.7*				

* The asterisks denote the crystallinity results of the freestanding octadecyl-passivated SiQDs, while those without asterisks represent the original crystallinity results within a SiO_2 matrix.

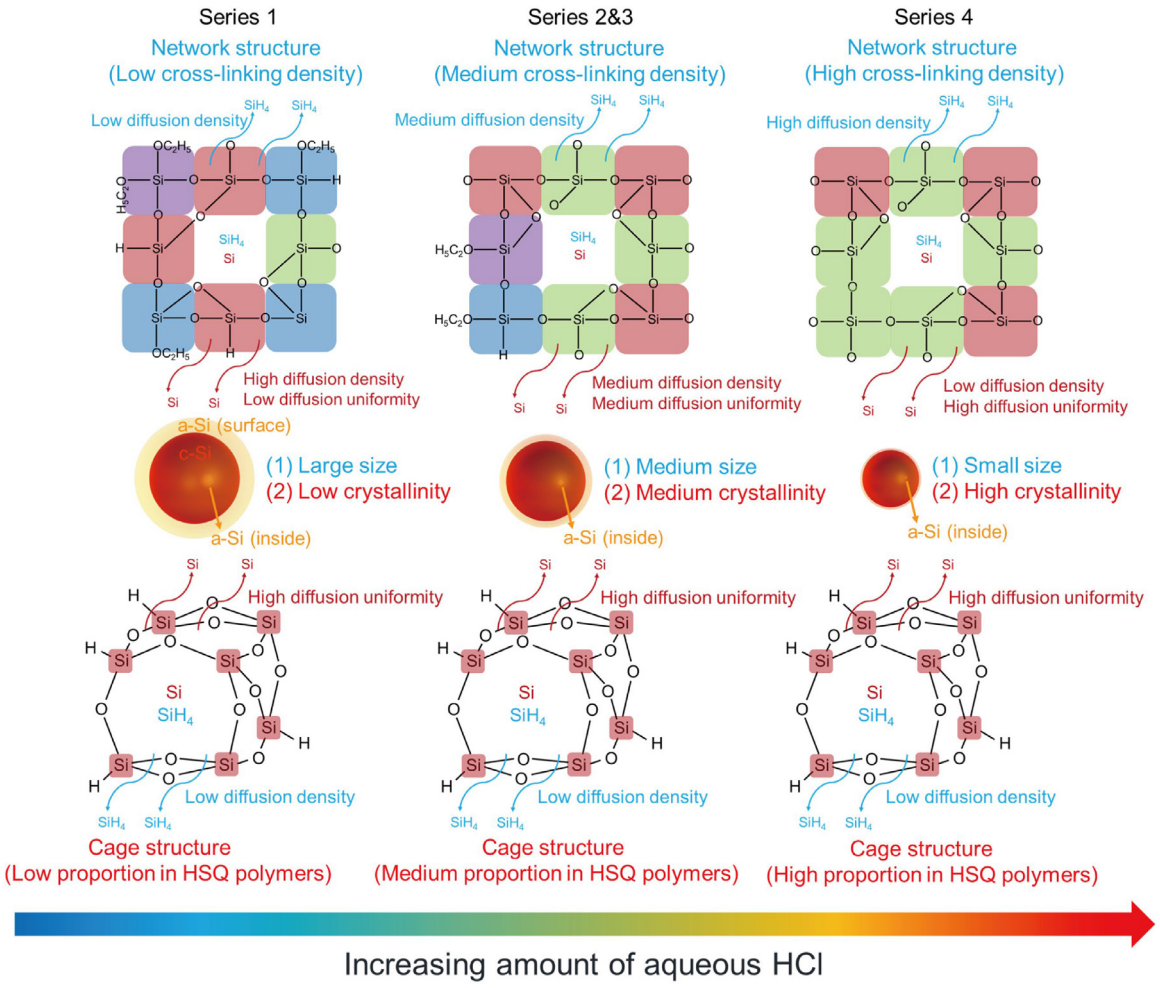

Fig. 11. Reaction mechanism for the formation of 1–4 series SiQDs by hydrolysis-pyrolysis process.

hydrolysis becomes sufficient, resulting in HSQ polymers that contain almost no groups 2 and 4. At this stage, the proportion of cage structures increases significantly. With the network structure primarily comprising groups 1 and 3, and with group 3 being predominant, the network exhibits a high cross-linking density and high diffusion uniformity. As a result, SiQDs with smaller size and higher crystallinity are formed. Overall, for the size of SiQDs, the cross-linking density of the network structure predominantly influences it, though the percentage of cage structure also plays a role. In terms of crystallinity, the cage structure provides a uniform diffusion barrier, while the network structure offers a relatively uniform diffusion barrier only when the siloxane cross-linking density is sufficiently high. A uniform diffusion barrier is crucial for preventing the formation of amorphous silicon. Therefore, the cage structure in HSQ polymers produced via hydrolysis serves as an excellent crystalline silicon precursor, while the network structure can only be classified as an effective crystalline silicon precursor under specific compositional conditions. It seems that utilizing HSQ polymers with predominantly cage structures may yield optimal results. However, two significant challenges persist: (1) the synthesis of HSQ polymers with nearly 100% cage structure purity is exceedingly difficult; and (2) a pure cage structure is associated with low diffusion barriers, leading to the formation of larger SiQDs. Therefore, a high proportion of cage structures, combined

with a network structure exhibiting high cross-linking density, facilitates the synthesis of SiQDs with both small size and high crystallinity.

4. Conclusions

In the synthesis of SiQDs from the pyrolysis of HSQ polymers, SiQDs with a size of 3.24 nm and a crystalline fraction of 98.4% were obtained by optimizing the TES/aqueous HCl volume ratio. The PL center wavelength of the SiQDs is 764.1 nm, exhibiting an average PLQY of 24.4%. We established that the proportions of cage structure and cross-linking density of network structure within TES-derived HSQ polymers can be regulated by the TES/aqueous HCl volume ratios. In regulating SiQD size, the cross-linking density of the network structure in the HSQ polymers plays a decisive role. A high cross-linking density results in high diffusion barriers, impeding the aggregation of silicon atoms necessary for SiQD formation. Consequently, these atoms may revert to SiH_4 and escape from the SiO_2 matrix, thereby limiting SiQD growth and resulting in the formation of smaller SiQDs. For the crystalline fraction, uniform diffusion of silicon atoms is critical for achieving high crystalline fraction. The cage structure, dominated by a single group ($HSiO_{1.5}$), provides a uniform diffusion barrier. The network structure, on the other hand, contains multiple groups, which result in non-uniform diffusion barriers. However, at elevated TES/aqueous HCl volume ratio, the composition of the groups within the network becomes increasingly homogeneous, leading to more uniform diffusion barriers. Thus, the cage structure is an excellent source of crystalline silicon, whereas the network structure serves as an effective source of crystalline silicon only at high cross-linking density. It is concluded that high crystalline fractions arise from both a high proportion of cage structures and a high cross-linking density of network structures. Overall, the cross-linking density of the network structure is crucial in controlling both the size and crystallinity of SiQDs. Our synthesis method allowed SiQDs to maintain outstanding crystalline fractions at relatively small sizes, achieving the highest crystalline fraction reported to date for HSQ polymer-derived SiQDs. This study aims to advance the application of small-sized SiQDs in lighting, display technologies, medical imaging, and photovoltaics.

Data availability statement

The data that support the findings of this study are available from the corresponding author upon reasonable request.

Declaration of competing interest

The authors declare that they have no known competing financial interests or personal relationships that could have appeared to influence the work reported in this paper.

CRediT authorship contribution statement

Yizhou He: Conceptualization, Data curation, Formal analysis, Investigation, Methodology, Writing – original draft, Writing – review & editing, Validation, Visualization, Software. **Qianxi Hao:** Data curation, Formal analysis, Investigation, Methodology, Validation. **Xue Yang:** Data curation, Formal analysis, Methodology, Resources, Supervision. **Jiamin Yu:** Formal analysis, Investigation. **Chi Zhang:** Formal analysis, Investigation. **Ruoyu Li:** Data curation, Investigation. **Qi Wang:** Data curation, Investigation. **Shaorong Li:** Resources, Supervision. **Xiaowei Guo:** Conceptualization, Data curation, Methodology, Project administration, Resources, Supervision, Validation, Writing – original draft, Writing – review & editing, Funding acquisition. **Serguei K. Lazarouk:** Investigation, Supervision.

Acknowledgements

This project was supported by the Sichuan Science and Technology Program (No. 2022ZYD0110) and the China National Tobacco Corporation Sichuan Company (No. SCYC202120). We would like to thank Dr. Yanying, Wang of the Analytical & Testing Center Sichuan University for her assistance with steady/transient fluorescence.

Supplementary materials

Supplementary material associated with this article can be found, in the online version, at doi:10.1016/j.jmst.2024.11.002.

References

[1] M.L. Mastronardi, F. Maier-Flaig, D. Faulkner, E.J. Henderson, C. Kübel, U. Lemmer, G.A. Ozin, Nano Lett. 12 (2012) 337–342.
[2] L.T. Canham, Appl. Phys. Lett. 57 (1990) 1046–1048.
[3] Z. Ni, S. Zhou, S. Zhao, W. Peng, D. Yang, X. Pi, Mater. Sci. Eng. R-Rep. 138 (2019) 85–117.
[4] B. Delley, E.F. Steigmeier, Phys. Rev. B 47 (1993) 1397–1400.
[5] M.J. De Castro, J.C. Pivin, J. Sol-Gel Sci. Technol. 28 (2003) 37–43.
[6] C.M. Hessel, E.J. Henderson, J.G.C. Veinot, Chem. Mater. 18 (2006) 6139–6146.
[7] N. Shirahata, T. Hasegawa, Y. Sakka, T. Tsuruoka, Small 6 (2010) 915–921.
[8] J.A. Kelly, E.J. Henderson, J.G.C. Veinot, Chem. Commun. 46 (2010) 8704–8718.
[9] M. Dasog, G.B. De los Reyes, L.V. Titova, F.A. Hegmann, J.G.C. Veinot, ACS Nano 8 (2014) 9636–9648.
[10] X. Liu, Y. Zhang, T. Yu, X. Qiao, R. Gresback, X. Pi, D. Yang, Part. Part. Syst. Char. 33 (2016) 44–52.
[11] E.J. Henderson, A.J. Shuhendler, P. Prasad, V. Baumann, F. Maier-Flaig, D.O. Faulkner, U. Lemmer, X.Y. Wu, G.A. Ozin, Small 7 (2011) 2507–2516.
[12] S. Chandra, B. Ghosh, G. Beaune, U. Nagarajan, T. Yasui, J. Nakamura, T. Tsuruoka, Y. Baba, N. Shirahata, F.M. Winnik, Nanoscale 8 (2016) 9009–9019.
[13] B. Ghosh, Y. Masuda, Y. Wakayama, Y. Imanaka, J. Inoue, K. Hashi, K. Deguchi, H. Yamada, Y. Sakka, S. Ohki, T. Shimizu, N. Shirahata, Adv. Funct. Mater. 24 (2014) 7151–7160.
[14] H. Yamada, N. Saitoh, B. Ghosh, Y. Masuda, N. Yoshizawa, N. Shirahata, J. Phys. Chem. C 124 (2020) 23333–23342.
[15] I.T. Cheong, J. Mock, M. Kallergi, E. Groß, A. Meldrum, B. Rieger, M. Becherer, J.G.C. Veinot, Adv. Opt. Mater. 11 (2023) 2201834.
[16] J. Watanabe, H. Yamada, H.T. Sun, T. Moronaga, Y. Ishii, N. Shirahata, Appl ACS Nano Mater. 4 (2021) 11651–11660.
[17] H. Yamada, J. Watanabe, K. Nemoto, H.T. Sun, N. Shirahata, Nanomaterials 12 (2022) 4314.
[18] Z. Deng, X.D. Pi, J.J. Zhao, D. Yang, J. Mater. Sci. Technol. 29 (2013) 221–224.
[19] F. Meinardi, S. Ehrenberg, L. Dhamo, F. Carulli, M. Mauri, F. Bruni, R. Simonutti, U. Kortshagen, S. Brovelli, Nat. Photon. 11 (2017) 177–185.
[20] X. Pi, Q. Li, D. Li, D. Yang, Sol. Energy Mater. Sol. Cells 95 (2011) 2941–2945.
[21] K. Saitow, T. Yamamura, J. Phys. Chem. C 113 (2009) 8465–8470.
[22] S. Wei, T. Yamamura, D. Kajiya, K. Saitow, J. Phys. Chem. C 116 (2012) 3928–3934.
[23] Y. Xin, K. Nishio, K. Saitow, Appl. Phys. Lett. 106 (2015) 201102.
[24] V. Svrcek, D. Mariotti, U. Cvelbar, G. Filipič, M. Lozac'h, C. McDonald, T. Tayagaki, K. Matsubara, J. Phys. Chem. C 120 (2016) 18822–18830.
[25] Y. Xin, T. Kitasako, M. Maeda, K. Saitow, Chem. Phys. Lett. 674 (2017) 90–97.
[26] A.V. Kabashin, A. Singh, M.T. Swihart, I.N. Zavestovskaya, P.N. Prasad, ACS Nano 13 (2019) 9841–9867.
[27] L. Mangolini, E. Thimsen, U. Kortshagen, Nano Lett. 5 (2005) 655–659.
[28] U.R. Kortshagen, R.M. Sankaran, R.N. Pereira, S.L. Girshick, J.J. Wu, E.S. Aydil, Chem. Rev. 116 (2016) 11061–11127.
[29] D. Jurbergs, E. Rogojina, L. Mangolini, U. Kortshagen, Appl. Phys. Lett. 88 (2006) 233116.
[30] A.G. Cullis, L.T. Canham, Nature 353 (1991) 335–338.
[31] Y. Kanemitsu, Phys. Rep. 263 (1995) 1–91.
[32] S. Lazarouk, P. Jaguiro, S. Katsouba, G. Maiello, S. La Monica, G. Masini, E. Proverbio, A. Ferrari, Thin Solid Films 297 (1997) 97–101.
[33] J.R. Heath, Science 258 (1992) 1131–1133.
[34] J. Zou, R.K. Baldwin, K.A. Pettigrew, S.M. Kauzlarich, Nano Lett. 4 (2004) 1181–1186.
[35] Q. Li, Y. He, J. Chang, L. Wang, H. Chen, Y.W. Tan, H. Wang, Z. Shao, J. Am. Chem. Soc. 135 (2013) 14924–14927.
[36] M. Rosso-Vasic, E. Spruijt, B. van Lagen, L. De Cola, H. Zuilhof, Small 4 (2008) 1835–1841.
[37] C.M. Hessel, D. Reid, M.G. Panthani, M.R. Rasch, B.W. Goodfellow, J. Wei, H. Fujii, V. Akhavan, B.A. Korgel, Chem. Mater. 24 (2012) 397–401.
[38] J.R. Rodríguez Núñez, J.A. Kelly, E.J. Henderson, J.G.C. Veinot, Chem. Mater. 24 (2012) 346–352.
[39] Y. Yu, C.E. Rowland, R.D. Schaller, B.A. Korgel, Langmuir 31 (2015) 6886–6893.
[40] M.A. Islam, M.H. Mobarok, R. Sinelnikov, T.K. Purkait, J.G.C. Veinot, Langmuir 33 (2017) 8766–8773.
[41] Y. Yu, G. Fan, A. Fermi, R. Mazzaro, V. Morandi, P. Ceroni, D.M. Smilgies, B.A. Korgel, J. Phys. Chem. C 121 (2017) 23240–23248.

[42] R.J. Clark, M. Aghajamali, C.M. Gonzalez, L. Hadidi, M.A. Islam, M. Javadi, M.H. Mobarok, T.K. Purkait, C.J.T. Robidillo, R. Sinelnikov, A.N. Thiessen, J. Washington, H. Yu, J.G.C. Veinot, Chem. Mater. 29 (2017) 80–89.
[43] I. Sychugov, A. Fucikova, F. Pevere, Z. Yang, J.G.C. Veinot, J. Linnros, ACS Photon. 1 (2014) 998–1005.
[44] J. Zhou, J. Huang, H. Chen, A. Samanta, J. Linnros, Z. Yang, I. Sychugov, J. Phys. Chem. Lett. 12 (2021) 8909–8916.
[45] A. Marinins, R. Zandi Shafagh, W. van der Wijngaart, T. Haraldsson, J. Linnros, J.G.C. Veinot, S. Popov, I. Sychugov, ACS Appl. Mater. Interfaces 9 (2017) 30267–30272.
[46] S. Terada, Y. Xin, K. Saitow, Chem. Mater. 32 (2020) 8382–8392.
[47] T. Ono, Y. Xu, T. Sakata, K. Saitow, ACS Appl. Mater. Interfaces 14 (2022) 1373–1388.
[48] M. Pauthe, E. Bernstein, J. Dumas, L. Saviot, A. Pradel, M. Ribes, J. Mater. Chem. 9 (1999) 187–191.
[49] E.J. Henderson, J.A. Kelly, J.G.C. Veinot, Chem. Mater. 21 (2009) 5426–5434.
[50] G.D. Sorarù, S. Modena, P. Bettotti, G. Das, G. Mariotto, L. Pavesi, Appl. Phys. Lett. 83 (2003) 749–751.
[51] G. Das, L. Ferraioli, P. Bettotti, F. De Angelis, G. Mariotto, L. Pavesi, E. Di Fabrizio, G.D. Soraru, Thin Solid Films 516 (2008) 6804–6807.
[52] Y. Xin, R. Wakimoto, K. Saitow, Chem. Mater. 46 (2017) 699–702.
[53] N. Shirahata, J. Nakamura, J. Inoue, B. Ghosh, K. Nemoto, Y. Nemoto, M. Takeguchi, Y. Masuda, M. Tanaka, G.A. Ozin, Nano Lett. 20 (2020) 1491–1498.
[54] M. Miyano, S. Endo, H. Takenouchi, S. Nakamura, Y. Iwabuti, O. Shiino, T. Nakanishi, Y. Hasegawa, J. Phys. Chem. C 118 (2014) 19778–19784.
[55] W.J.I. DeBenedetti, S.K. Chiu, C.M. Radlinger, R.J. Ellison, B.A. Manhat, J.Z. Zhang, J. Shi, A.M. Goforth, J. Phys. Chem. C 119 (2015) 9595–9608.
[56] B. Ghosh, T. Hamaoka, Y. Nemoto, M. Takeguchi, N. Shirahata, J. Phys. Chem. C 122 (2018) 6422–6430.
[57] M.L. Mastronardi, F. Hennrich, E.J. Henderson, F. Maier-Flaig, C. Blum, J. Reichenbach, U. Lemmer, C. Kübel, D. Wang, M.M. Kappes, G.A. Ozin, J. Am. Chem. Soc. 133 (2011) 11928–11931.
[58] K. Fujimoto, T. Hayakawa, Y. Xu, N. Jingu, K. Saitow, ACS Sustainable Chem. Eng. 10 (2022) 14451–14463.
[59] H. Ueda, K. Saitow, ACS Appl. Mater. Interfaces 16 (2024) 985–997.
[60] K. Saitow, Bull. Chem. Soc. Jpn. 97 (2024) uoad002.
[61] Y. Xu, Y. Xin, K. Kato, T. Shirai, J Mater. Chem. C 10 (2022) 12588–12601.
[62] N. Jingu, K. Sumida, T. Hayakawa, T. Ono, K. Saitow, Chem. Mater. 36 (2024) 5077–5091.
[63] S. Hernández, J. López-Vidrier, L. López-Conesa, D. Hiller, S. Gutsch, J. Ibáñez, S. Estradé, F. Peiró, M. Zacharias, B. Garrido, J. Appl. Phys. 115 (2014) 203504.
[64] E. Bustarret, M.A. Hachicha, M. Brunel, Appl. Phys. Lett. 52 (1988) 1675–1677.
[65] T. Mizutani, H. Ohta, T. Ueda, T. Kashiwagi, T. Fukuda, T. Shiobara, K. Saitow, ACS Sustainable Chem. Eng. 11 (2023) 11769–11780.
[66] A.N. Thiessen, L. Zhang, A.O. Oliynyk, H. Yu, K.M. O'Connor, A. Meldrum, J.G.C. Veinot, Chem. Mater. 32 (2020) 6838–6846.
[67] I.T. Cheong, L. Yang Szepesvari, C. Ni, C. Butler, K.M. O'Connor, R. Hooper, A. Meldrum, J.G.C. Veinot, Nanoscale 16 (2024) 592–603.
[68] G. Viera, S. Huet, L. Boufendi, J. Appl. Phys. 90 (2001) 4175–4183.
[69] T.C. Paul, J. Podder, Appl. Phys. A 125 (2019) 818.
[70] A. Khorsand Zak, W.H. Abd. Majid, M.E. Abrishami, R. Yousefi, Solid State Sci. 13 (2011) 251–256.
[71] Z. Ni, X. Pi, M. Ali, S. Zhou, T. Nozaki, D. Yang, J. Phys. D-Appl. Phys. 48 (2015) 314006.
[72] T. van Buuren, L.N. Dinh, L.L. Chase, W.J. Siekhaus, L.J. Terminello, Phys. Rev. Lett. 80 (1998) 3803–3806.
[73] J.W. Luo, S.S. Li, I. Sychugov, F. Pevere, J. Linnros, A. Zunger, Nat. Nanotechnology 12 (2017) 930–932.
[74] W. de Boer, D. Timmerman, I. Yassievich, A. Capretti, T. Gregorkiewicz, Nat. Nanotechnol. 12 (2017) 932–933.
[75] L. Canham, Faraday Discuss. 222 (2020) 10–81.
[76] C.S. Yang, R.A. Bley, S.M. Kauzlarich, H.W.H. Lee, G.R. Delgado, J. Am. Chem. Soc. 121 (1999) 5191–5195.
[77] K.Y. Cheng, R. Anthony, U.R. Kortshagen, R.J. Holmes, Nano Lett. 11 (2011) 1952–1956.
[78] S. Ma, T. Yue, X. Xiao, H. Cheng, D. Zhao, J. Lumin. 201 (2018) 77–84.
[79] D.P. Puzzo, E.J. Henderson, M.G. Helander, Z. Wang, G.A. Ozin, Z. Lu, Nano Lett. 11 (2011) 1585–1590.
[80] Q. He, K. Wang, D. Li, D. Yang, X. Pi, Adv. Opt. Mater. 12 (2024) 2302422.
[81] J.C. de Mello, H.F. Wittmann, R.H. Friend, Adv. Mater. 9 (1997) 230–232.
[82] J. Zhou, F. Ma, K. Chen, W. Zhao, R. Yang, C. Qiao, H. Shen, W.S. Su, M. Lu, Y. Zheng, R. Zhang, L. Chen, S. Wang, Nanoscale Adv. 5 (2023) 3896–3904.
[83] H. Sugimoto, M. Yamamura, R. Fujii, M. Fujii, Nano Lett. 18 (2018) 7282–7288.
[84] H. Yamada, N. Shirahata, Micromachines 10 (2019) 318.
[85] İ.N.G. Özbilgin, B. Ghosh, H. Yamada, N. Shirahata, J. Phys. Chem. C 125 (2021) 3421–3431.